

1
2
3
4
5
6
7
8
9
10
11
12
13
14
15
16
17
18
19
20
21

Linear wind-forced beta-plumes with application to the Hawaiian Lee Countercurrent

Ali Belmadani^{1,2}, Nikolai A. Maximenko¹, Julian P. McCreary^{1,3}, Ryo Furue¹, Oleg V. Melnichenko¹, Niklas Schneider^{1,3}, and Emanuele Di Lorenzo⁴

¹ International Pacific Research Center, School of Ocean and Earth Science and Technology, University of Hawaii at Manoa, Honolulu, Hawaii

² Department of Geophysics, Faculty of Physical and Mathematical Sciences, Universidad de Concepcion, Concepcion, Chile

³ Department of Oceanography, School of Ocean and Earth Science and Technology, University of Hawaii at Manoa, Honolulu, Hawaii

⁴ School of Earth and Atmospheric Sciences, Georgia Institute of Technology, Atlanta, Georgia

In revision for the *Journal of Physical Oceanography*

April 30th, 2013

Corresponding author address: Ali Belmadani, DGEO, FCFM, Universidad de Concepcion, Avda. Esteban Iturra s/n - Barrio Universitario, Casilla 160-C, Concepcion, Chile. E-mail: abelmadani@dgeo.udec.cl.

22 **Abstract**

23 Two numerical ocean models are used to study the baroclinic response to forcing by
24 localized wind-stress curl (i.e., a wind-forced β -plume, which is a circulation cell developing to
25 the west from the source region and comprised of a set of zonal jets) with implication to the
26 Hawaiian Lee Countercurrent (HLCC): an idealized primitive-equation model (ROMS), and a
27 global, eddy-resolving, general circulation model (OFES). In addition, theoretical ideas inferred
28 from a linear continuously-stratified model are used to interpret results. In ROMS, vertical
29 mixing preferentially damps higher-order vertical modes. The damping thickens the plume west
30 of the forcing region, weakening the near-surface zonal jets and generating deeper zonal
31 currents. The zonal damping scale increases monotonically with the meridional forcing scale,
32 indicating a dominant role of vertical viscosity over diffusion, a consequence of the small forcing
33 scale. In the OFES run forced by NCEP reanalysis winds, the HLCC has a vertical structure
34 consistent with that of idealized β -plumes simulated by ROMS, once the contribution of the
35 North Equatorial Current (NEC) has been removed. Without this filtering, a deep HLCC branch
36 appears artificially separated from the surface branch by the large-scale intermediate-depth NEC.
37 The surface HLCC in two different OFES runs exhibits sensitivity to the meridional wind curl
38 scale that agrees with the dynamics of a β -plume in the presence of vertical viscosity. The
39 existence of a deep HLCC extension is also suggested by velocities of Argo floats.

40

41

42 **1. Introduction**

43 *1.1 Background*

44 *1.1.1 Definition of a β -plume:* A β -plume (Rhines 1994) is the anisotropic large-scale ocean
45 circulation induced by a localized vorticity source (associated with fluxes of momentum, heat, or
46 mass). The basic dynamics of β -plumes can be described with linear models that allow for
47 analytical solutions (Stommel 1982; Pedlosky 1996). In such models, the steady-state response to
48 a localized patch of wind curl is a zonally-elongated gyre consisting of a pair of zonal jets
49 extending west of the forcing region, which is established by the westward radiation of
50 barotropic and baroclinic Rossby waves.

51 *1.1.2 Small-scale patches of wind curl:* Compact vorticity sources arising from small-scale
52 wind stress curl are present in many regions of the world ocean (Chelton et al. 2004). They can
53 appear at the oceanic mesoscale as a result of air-sea interaction over SST fronts (e.g., Small et
54 al. 2008), surface currents (Cornillon and Park 2001; Kelly et al. 2001), or from orographic
55 effects near coastlines and islands (Xie et al. 2001; Jiménez et al. 2008). The resulting patterns of
56 small-scale wind curl differ markedly, from monopoles (e.g., next to the coast) and dipoles (e.g.,
57 next to an island) to more complicated structures (e.g., in the Southern Ocean), on horizontal
58 scales from 10–1000 km (Chelton et al. 2004). It has been hypothesized that the Hawaiian Lee
59 Countercurrent (HLCC) (Qiu et al. 1997) may be interpreted as a prominent example of a β -
60 plume forced by such winds: the tall volcanoes of the island of Hawaii block the trade winds,
61 inducing a small-scale wind-stress-curl dipole downstream from the island; it generates the
62 narrow near-surface HLCC, which flows eastward against the large-scale westward North
63 Equatorial Current (NEC) (Xie et al. 2001).

64 *1.1.3 Previous studies:* Previous studies of β -plume dynamics have used barotropic
65 (Haidvogel and Rhines 1983; Waterman and Jayne 2012), reduced-gravity (Davey and Killworth
66 1989; Özgökmen et al. 2001), or other simplified models with a small number of vertical layers

67 (Spall 2000; Kida et al. 2008, 2009). Although such models can simulate basic β -plume features,
68 they are not able to simulate its vertical structure realistically because of their limited vertical
69 resolution.

70 *1.2 Present research*

71 In this paper, we investigate the vertical structure of β -plumes using two numerical models:
72 the Regional Oceanic Modeling System (ROMS) (Shchepetkin and McWilliams 2005;
73 Haidvogel et al. 2008), forced with an idealized, small-scale wind pattern with a quasi-monopole
74 curl; and the Ocean general circulation model for the Earth Simulator (OFES) (Masumoto et al.
75 2004). The former model is useful for isolating basic physics, and the latter to provide
76 simulations of the HLCC that are as realistic as possible. To help with the dynamical
77 interpretation of the numerical results, we use theoretical ideas inferred from a linear
78 continuously stratified (LCS) model. Finally, to check the realism of the OFES solutions, we
79 compare them with observations of surface and deep flow derived from trajectories of Argo
80 floats (Lebedev et al. 2007).

81

82 **2. Models and Data**

83 Idealized solutions are obtained using ROMS, which solves the hydrostatic primitive
84 equations with stretched sigma-coordinates on 32 vertical levels. ROMS is used at a resolution of
85 $1/12^\circ$ in a closed rectangular subtropical domain (20°N – 40°N , 60° zonal extent) with a flat
86 bottom of depth $H = 4000$ m. Each run starts from no motion and from horizontally-uniform
87 stratification typical for the eastern part of the North Pacific subtropical gyre (Antonov et al.
88 2010; Locarnini et al. 2010). Subgrid-scale vertical mixing is parameterized by constant
89 Laplacian viscosity ($\nu = 10^{-4} \text{ m}^2\text{s}^{-1}$) and diffusivity ($\kappa = 10^{-5} \text{ m}^2\text{s}^{-1}$). A 50 km-wide sponge layer

90 is used along the lateral boundaries to resolve the western boundary Munk layer and to damp
91 Kelvin waves. Horizontal viscosity and diffusivity increase linearly within the sponge layer from
92 zero at the interior to $700 \text{ m}^2\text{s}^{-1}$ along the solid boundaries. There is no explicit horizontal mixing
93 outside the sponge layer; the model relies on a third-order upstream-biased advection operator
94 for horizontal mixing.

95 The idealized model is forced at the surface with a steady anticyclonic wind vortex generated
96 by a Gaussian streamfunction located in the center of the domain (Figs. 1a, 1b, appendix A),
97 giving a maximum wind stress of $\tau_{max} = 10^{-5} \text{ N m}^{-2}$ at a distance $R = 40 \text{ km}$ from the vortex
98 center, which corresponds to a typical value for the deformation radius of the first baroclinic
99 mode at 30°N in the eastern Pacific (Chelton et al. 1998). Such a weak forcing ensures that the
100 model remains in a linear regime, that is, the horizontal advection terms are insignificant and the
101 formation of eddies is prevented. The associated curl consists of a negative central region
102 surrounded by a weaker positive ring, a quasi-monopole (Fig. 1b, appendix A). Since the system
103 is linear, the response to an arbitrary compact forcing (dipole, band, etc.) can be expressed as a
104 linear combination of the responses to monopoles of this sort. Heat and freshwater fluxes are set
105 to zero. The time step of the integration is 20 min for the baroclinic response and 20 s for the
106 barotropic mode. Simulations are run for 10 years after a 20-year spin-up, by which time they are
107 close to a steady state.

108 The baroclinic structure of the HLCC is investigated by analyzing two solutions to OFES as
109 well as currents estimated from Argo data. OFES is a global eddy-resolving (0.1°) model with 54
110 vertical levels and with vertical mixing parameterized using the KPP scheme (Large et al. 1994).
111 As in Sasaki and Nonaka (2006), we compare OFES simulations forced by the NCEP-NCAR
112 reanalysis (Kalnay et al. 1996) winds (OFES-N) and by the QuikSCAT satellite winds (OFES-

113 Q), offering more spatial details, for the time period 1999–2008. Observed surface and deep
114 (~1000 m) HLCC velocities are estimated from trajectories of 4284 Argo floats over 1997–2007,
115 bin-averaged on a global 1° grid (YoMaHa’07 data – Lebedev et al. 2007). In addition to mean
116 velocities, the dataset contains values of standard deviation and data density. Uncertainties in the
117 velocity estimates are substantial and are discussed in appendix B.

118

119 3. Results

120 3.1 Idealized β -plume

121 The strength of the linear, inviscid β -plume is set by the Sverdrup balance (Sverdrup 1947),

$$122 \quad \beta \frac{\partial \Psi}{\partial x} = \mathbf{k} \cdot \frac{\nabla \times \boldsymbol{\tau}}{\rho_b} \quad , \quad (1)$$

123 where β is the meridional gradient of the Coriolis parameter f , Ψ is the barotropic streamfunction,
124 $\boldsymbol{\tau}$ is the surface wind stress, and ρ_b is the average density of the water column in the study
125 region. As shown in Appendix A, the barotropic circulation that forms in response to the
126 localized anticyclonic wind vortex (A3) consists of three β -plume cells: a main anticyclonic cell
127 aligned with the vortex center, and two weaker cyclonic cells on its flanks (Fig. 2a). Four zonal
128 jets, fringing these cells, extend from the forcing area to the western boundary. Since (1) holds
129 outside the sponge layer along the western boundary, the barotropic flow of the numerical
130 solution (Fig. 2b) agrees well with the analytical solution (Fig. 2a). West of the forcing region,
131 the flow is purely zonal and independent of longitude in accordance with (1).

132 Unlike the barotropic transport, the surface jets decay westward (Fig. 2c). The decay is due to
133 the momentum redistribution between the upper ocean and the interior. Indeed, the bottom of the
134 main eastward jet deepens with distance from the source, leading to the emergence of deep flow
135 far from the forcing region (Fig. 3a; see also Fig. 2d) and to a reduction in vertical shear.

136 *3.2 Application to the HLCC*

137 *3.2.1 OFES solutions:* Similar to the idealized β -plume (Fig. 2c), the HLCC surface flow
138 features a westward decay in both OFES simulations (Figs. 4a, 4b, see also Figs. 8c, 8d). A
139 notable difference between the two solutions is the HLCC zonal extent: whereas the surface
140 HLCC does not appear to extend beyond $\sim 175^\circ\text{W}$ in OFES-Q (Fig. 4b), in agreement with
141 surface drifter data (Qiu et al. 1997; Yu et al. 2003; Lumpkin and Flament 2013), it extends
142 much further west in OFES-N, as evidenced by the patches of eastward current found along the
143 HLCC axis between 150°E – 155°E and the dateline (Fig. 4a). As shown in section 4, these
144 differences may be partly due to the horizontal scale of the forcing.

145 Regarding the vertical structure of the flow west of Hawaii along the HLCC axis, both
146 simulations have the eastward-flowing HLCC in the upper ~ 200 m depth with maximum
147 velocities $6\text{--}8\text{ cm s}^{-1}$; it lies on top, and to the east, of the westward-flowing NEC, which extends
148 down to ~ 600 m depth, with maximum velocities exceeding 10 cm s^{-1} near the western boundary
149 and with weaker currents of $1\text{--}2\text{ cm s}^{-1}$ east of 170°E (Figs. 5a, 6a). These results are in
150 agreement with the geostrophic velocities derived between 170°E and 160°W by Yoshida et al.
151 (2011) from Argo hydrographic data over 2005–2009. Note that the HLCC core is located below
152 the surface at ~ 30 m depth in both simulations and tends to extend farther west compared to its
153 surface signature (see the thin layer of near-surface westward flow on Figs. 5a, 6a), to 130°E –
154 140°E for OFES-N and 140°E – 150°E for OFES-Q (horizontal maps not shown) instead of
155 150°E – 155°E for OFES-N and $\sim 175^\circ\text{W}$ for OFES-Q at the surface (Fig. 4); this westward extent
156 is in agreement with the hydrographic data of Kobashi and Kawamura (2002) and of Aoki et al.
157 (2002), which indicate the presence of the HLCC west of the dateline.

158 On the other hand, the OFES simulations have a weak ($0.5\text{--}1\text{ cm s}^{-1}$) eastward flow below
159 the NEC (Figs. 5a, 6a), which is absent from previous observational studies that lack deep flow
160 observations. In OFES-N, this deep current seems to originate a few degrees to the west of the
161 Hawaiian Islands, underneath the HLCC at its location of maximum velocity, and deepens
162 toward the west; for example, the 0.5 cm s^{-1} contour reaches depths of $1000\text{--}1200\text{ m}$ near 140°E
163 (Fig. 5a). In OFES-Q, the two currents are separated by westward flow near $\sim 163^\circ\text{W}$ (Fig. 6a).
164 The subsurface eastward current appears to continue east of Hawaii and to shoal until it reaches
165 the near surface at the basin eastern boundary, near the coast of Mexico in both simulations
166 (Figs. 5a, 6a), challenging the hypothesis of an island-induced flow. Still, there is a clear step in
167 the deep flow magnitude in OFES-N, from $0\text{--}0.5\text{ cm s}^{-1}$ east of Hawaii to $0.5\text{--}1\text{ cm s}^{-1}$ west of
168 the islands (Fig. 5a), which suggests a contribution of the HLCC β -plume. Although not as
169 marked, there is also a jump in OFES-Q (Fig. 6a), as indicated by the vertical extent of the 0.5
170 cm s^{-1} closed contours that is smaller to the east ($\sim 150\text{ m}$) compared to the west ($\sim 400\text{ m}$) of the
171 islands.

172 In fact, the connection between the deep flow and the surface HLCC in both OFES
173 simulations is best revealed by removing the large-scale NEC flow. Indeed, to extract the narrow
174 HLCC signal from the OFES-N (OFES-Q) solution, we isolate it from the broad NEC using a
175 high-pass filter in y with a Hann window of 10° (6°) half-width. This filtering allows for the
176 HLCC to be compared more easily to the idealized experiments presented in section 3.1, which
177 do not contain any background flow. The different filter widths chosen for the two OFES
178 solutions are related to the different HLCC meridional scales, which are related to different
179 scales of the wind products (see below).

180 High-pass filtered zonal currents reproduce the main characteristic features of the idealized
181 baroclinic β -plumes (Figs. 5c, 6c): westward reduction in vertical shear, decay of surface flow
182 (see also Figs. 8c, 8d), emergence of deep flow (extending down to 1000–1200 m as indicated by
183 the 0.5 cm s^{-1} contours on Figs. 5c, 6c) to the west of the island (see also Fig. 7b), and in OFES-
184 N, westward deepening of the eastward flow (evidenced by the 0.5 cm s^{-1} and 1 cm s^{-1} contours
185 on Fig. 5c). Note the similarity of the high-pass filtered and unfiltered deep flows on Figs. 5 and
186 6, which reflects the absence of large-scale flow below $\sim 600 \text{ m}$ (Figs. 5b, 6b) and excludes the
187 possibility that the deep flow may be an artifact due to spatial filtering. However, the NEC signal
188 is not removed completely at intermediate depths, as can be seen on Figs. 5c, 6c from a layer of
189 lower eastward velocities around 400 m depth (veering westward near the Asian coast),
190 extending roughly from the western boundary to the dateline. This limits to some extent our
191 interpretation, although the striking similarity between the ROMS and OFES-N model results
192 suggests it is not a critical issue.

193 In OFES-Q, the deep flow appears to achieve its maximum directly below or possibly even to
194 the east of the maximum near-surface flow and remains at a constant depth far to the west (see
195 the 0.5 cm s^{-1} contour on Fig. 6c; see also Figs. 7a, 7b), unlike the idealized model. An apparent
196 core of the subsurface eastward flow seems to be deepening when looking at unfiltered data (Fig.
197 6a), but this is deceptive since this feature is due to the superimposition of the constant-depth
198 deep eastward flow (Fig. 6c) with the deepening westward-flowing NEC (Fig. 6b). Yet, the
199 presence of the subsurface eastward flow seems to be related to the presence of the island and
200 possibly the HLCC. Indeed, while large horizontal scales show coherent flow structure at all
201 depths across the basin (Fig. 6b), small meridional scales show distinct structures on both sides
202 of the island (Fig. 6c). The eastward flow found east of Hawaii that deepens westward is much

203 weaker than its counterpart found west of Hawaii and changes sign on multiple occasions, unlike
204 the latter (Fig. 6c). In addition, it is capped by weak westward flow that also deepens westward,
205 but is not found west of the island. As expected, any eastward surface flow found to the east of
206 Hawaii is much weaker than the HLCC. The discrepancy between the deep flows in OFES-Q on
207 the one hand and in both OFES-N and the idealized model on the other hand may be the result of
208 air-sea interaction or nonlinear dynamics (see below).

209 The figures also reveal that the surface jets extend as far west as $\sim 130^\circ\text{E}$, but are significantly
210 weaker west of $\sim 170^\circ\text{W}$ in both runs (Figs. 5c, 6c). This decay is consistent with Sasaki and
211 Nonaka (2006), who reported the HLCC termination in OFES near the dateline. Noteworthy,
212 whereas the maximum eastward velocity of the near-surface HLCC is located at about $\sim 30\text{m}$
213 depth in the unfiltered data (Figs. 5a, 6a), it is located right at the surface in the meridionally-
214 filtered data (Figs. 5c, 6c). On the other hand, there is a very thin layer of intensified westward
215 flow (purple color) very close to the surface in the low-pass-filtered data (Figs. 5b, 6b). These
216 features are likely due to large-scale near-surface Ekman drift, which has a slight westward
217 component associated with the northeasterly trade winds (not shown). On the other hand, the
218 surface current zonal decay scale is shorter in OFES-Q (Fig. 6c) than in OFES-N (Fig. 5c). This
219 is particularly obvious in horizontal maps of the high-pass filtered surface flows (Figs. 8c, 8d).

220 To further show that the deep eastward flow below the HLCC in OFES-Q is related to the
221 presence of the island and hence likely a deep HLCC extension, horizontal maps of high-pass
222 filtered surface and deep flows are shown in Figs. 7a, 7b. From these figures, it is clear that while
223 zonally coherent eastward flow is found along the HLCC axis west of Hawaii both at the surface
224 and 1000 m depth, no such coherence is found to the east. Some striated pattern resembling
225 features previously found in both observations (Maximenko et al. 2008) and numerical models

226 (Centurioni et al. 2008; Melnichenko et al. 2010) may be seen east of the island, but they are
227 weaker, noisier, and not aligned with the HLCC.

228 Figs. 8a and 8b show the 1999–2008 mean barotropic zonal transport per unit width in
229 OFES-N and OFES-Q, respectively, after the high-pass filtering is applied. Consistent with the
230 Sverdrup dynamics, both runs exhibit zonally-stretched cyclonic and anticyclonic circulations
231 west of the island of Hawaii, aligned with the regions of positive and negative wind stress curl
232 (white contours), respectively; these circulations give rise to the HLCC between them and
233 strengthen the NEC on the outer flanks. The wind-stress-curl dipole is much broader and
234 somewhat weaker in the coarse NCEP wind data compared to the higher-resolution QuikSCAT
235 data (Figs. 8a, 8b), as previously noted by Sasaki and Nonaka (2006). As a result, the HLCC
236 meridional scale is larger for OFES-N ($\sim 3^\circ$) compared to OFES-Q ($\sim 2^\circ$).

237 One discrepancy between the OFES HLCC and the idealized β -plume is the relative decay of
238 the barotropic and surface flows. In the idealized model, the surface flow decays westward,
239 while the barotropic flow extends to the western boundary without decay (Fig. 2). Although
240 stretching over distances of several thousand kilometers, the HLCC barotropic transport decays
241 westward in the OFES simulations, particularly in OFES-Q (Figs. 8a, 8b; see also Fig. 10). In
242 OFES-N, although the barotropic flow drops steeply by $\sim 40\%$ near 165°W , it is nearly zonally-
243 uniform between 165°W and 170°E (Fig. 8a), while the surface flow decays by $\sim 60\%$ over the
244 same longitude range (Fig. 8c), similar to the idealized β -plume (Fig. 2b). The analogy with the
245 latter is limited west of 170°E where the OFES-N barotropic flow encounters a meridionally-
246 oriented topographic barrier (not shown) and drops again by $\sim 50\%$ (possibly as a result of
247 topographic steering and associated vortex stretching, which are not represented in the idealized
248 model), while the surface flow appears undisturbed (Figs. 8a, 8c). In contrast, in OFES-Q both

249 the zonal transport of the HLCC and the surface flow decay westward from about 160°W to
250 180°E with approximately the same rate and are slightly tilted southwestward (Figs. 8b, 8d). As
251 shown below, the former feature is likely due to the QuikSCAT wind stress curl pattern and
252 underlying air-sea interaction in the far field, which is absent in the NCEP data (Xie et al. 2001;
253 Sasaki and Nonaka 2006), while the latter feature may be the result of nonlinear stress, including
254 eddy fluxes.

255 Two processes contributing to the barotropic flow but not represented in the idealized model
256 may be responsible for the discrepancy between the OFES and ROMS solutions. On the one
257 hand, non-zero wind stress curl forcing west of Hawaii can modify the Sverdrup flow in the far-
258 field (Xie et al. 2001). On the other hand, the HLCC is dominated by mesoscale eddies (Holland
259 and Mitchum 2001; Calil et al. 2008; Yoshida et al. 2010; Jia et al. 2011), which may contribute
260 to its early termination via horizontal mixing (Yu et al. 2003) and/or vertical momentum transfer
261 due to eddy form stress, which are not taken into account here.

262 The eddy kinetic energy (EKE) fields of the OFES-N and OFES-Q solutions are
263 represented in Figs. 9a and 9b, respectively. Eddy activity along the HLCC is of the same order
264 in the run forced by QuikSCAT as that in the run forced by NCEP, if not slightly weaker. This
265 property suggests that eddy-induced horizontal mixing may not be responsible for the shorter
266 extent of the barotropic flow in OFES-Q.

267 Fig. 10 represents the total transports west of Hawaii in OFES-N and OFES-Q, as well as
268 those computed from the NCEP and QuikSCAT wind-stress-curl fields, using the Sverdrup
269 balance (1) and the depth-integrated continuity equation (A4). Both the total transports and the
270 wind stress curls have been meridionally high-pass filtered, with the filter characteristics
271 presented earlier, in order to focus on scales relevant to the HLCC barotropic flow and forcing

272 fields. After a sharp increase in the island lee where the forcing is located, the Sverdrup zonal
273 transport per unit width induced by the NCEP winds (thick solid line) increases more
274 progressively between $\sim 165^\circ\text{W}$ and $\sim 160^\circ\text{E}$ before reaching an almost constant value of ~ 33
275 m^2s^{-1} farther west. This results from a weak quasi-zonal wake extending the NCEP wind-stress
276 curl Hawaii dipole westward to $\sim 160^\circ\text{E}$, and from the absence of coherent small-scale wind
277 structures in the region farther west (not shown). In the absence of small-scale structures in the
278 NCEP coarse-resolution SST forcing, the wind-stress-curl wake is likely the sole result of the
279 low-level flow perturbation by the Hawaiian orography.

280 In contrast, the Sverdrup zonal transport per unit width forced by the QuikSCAT winds
281 (thick dashed line on Fig. 10) increases from the island lee to $\sim 170^\circ\text{W}$ where it reaches a
282 maximum of $\sim 43 \text{ m}^2\text{s}^{-1}$, and then decreases progressively westward by 35–40%, down to 26–27
283 m^2s^{-1} at $130\text{--}140^\circ\text{E}$. The larger Sverdrup transport in the island lee in OFES-Q is due to the
284 stronger and meridionally-narrower wind stress curl compared to OFES-N (Figs. 8a, 8b). The
285 decrease west of $\sim 170^\circ\text{W}$ results from a southwestward shift of the zonally-elongated
286 QuikSCAT wind-stress-curl dipole (not shown). Hence, at the latitude of the island of Hawaii,
287 both the curl and its meridional gradient change sign rapidly in the westward direction due to this
288 tilt. This implies a westward weakening of Sverdrup zonal transport. The tilt in the curl dipole
289 results partly from air-sea interaction over the HLCC caused by the eastward advection of
290 western Pacific warm waters, which tends to extend the dipole in the far-field where the HLCC
291 axis is also tilted meridionally (Xie et al. 2001; Sasaki and Nonaka 2006). Such air-sea coupling
292 over the warm HLCC tongue is not represented in NCEP but is captured by QuikSCAT.
293 However, the linear Sverdrup response itself is not responsible for the tilt in the HLCC because
294 the far-field curl dipole is too weak to generate eastward Sverdrup flow to the south (not shown).

295 Thus, the tilt in the HLCC is likely due to nonlinear stress associated with the background flow,
296 eddies, and/or topographic steering (Kessler et al. 2003).

297 The total HLCC barotropic transports in OFES-N (thin solid line on Fig. 10) and OFES-
298 Q (thin dashed line) are entirely explained by the Sverdrup response in the island lee until 160–
299 165°W where they reach their respective maxima, before decaying westward as a result of
300 nonlinear effects. The faster decay in OFES-Q appears qualitatively consistent with the wind-
301 curl pattern to the west of Hawaii in the QuikSCAT winds, although it is possible that
302 differences in eddy fluxes between the two simulations also play a role. With similar large-scale
303 winds in NCEP and QuikSCAT (not shown) and the same bottom topography in the two OFES
304 runs, it is unlikely that advection by the background flow and topographic steering play any
305 significant role in the faster decay of the OFES-Q barotropic flow.

306 However, the OFES-Q barotropic flow decreases not only due west but also upstream
307 (southwestward) along the tilted HLCC (Fig. 8b, thin dotted line on Fig. 10). Unlike the region
308 further north, the transport west of ~160°E along the tilted HLCC is directed eastward (compare
309 thin dashed and dotted lines on Fig. 10). The Sverdrup flow taken along the same tilted axis also
310 decays west of ~165°W with a similar, although perhaps slightly faster decay rate (thick dotted
311 line) compared to the total transport (thin dotted line). Compared to the Sverdrup flow taken
312 along the 18.5–19.5°N latitude band (thick dashed line), that taken along the tilted HLCC is
313 twice weaker at most and decays faster (thick dotted line). That is because the Sverdrup flow is
314 almost purely zonal and flows westward south of ~18.5°S (not shown). Thus, its slightly faster
315 decay along the tilted HLCC compared to total transport suggests that nonlinear stress may be
316 responsible for the tilt and may act to reduce the decay induced by the far-field small-scale wind
317 pattern. Further studies will be needed in order to test this hypothesis.

318 The baroclinic β -plume generated by the QuikSCAT curl pattern west of Hawaii that is
319 acting in opposition to the dipole in the island lee may partially cancel the deep eastward flow
320 below the HLCC. This may explain the different vertical structure of the HLCC in OFES-Q
321 (Fig.6c) compared to that in OFES-N (Fig.5c). On the other hand, it also possible that differences
322 in nonlinear stress between the two simulations, eddy fluxes in particular, play a role in these
323 differences in the baroclinic flow structure.

324 3.2.2 *Observations:* The YoMaHa'07 ensemble-mean zonal velocities, derived from
325 trajectories of Argo floats and filtered with the high-pass filter used for OFES-Q, are used to
326 assess the observed HLCC vertical structure. Whereas the surface jet is strongest in the lee of
327 Hawaii (Fig. 7c), deep current is weak there but appears west of $\sim 165^\circ\text{E}$ as a quasi-zonal jet
328 extending $15\text{--}20^\circ$ in the zonal direction (Fig. 7d). Despite the large error in deep velocity
329 estimates (Fig. B2c), the presence of a coherent zonal band in the deep flow standard deviation
330 between 140°E and 175°E (Fig. B2b) suggests that the deep eastward flow aligned with the
331 surface HLCC axis is not a sampling artifact. The data appears qualitatively consistent with the
332 idealized model (Figs. 2c, 2d), with a surface flow decay and a deep flow strengthening in the
333 westward direction (Figs. 7c, 7d), which may be a deep extension of the HLCC. However, as one
334 might expect given all the limitations of the YoMaHa'07 data (appendix B), the quantitative
335 agreement between the deep flows in YoMaHa'07 and OFES-Q is poor and the comparison is
336 complicated by noise and multiple local maxima (Figs. 7b, 7d). It should be noted in particular
337 that interpolation artifacts in the YoMaHa'07 data may introduce noise in the meridionally high-
338 pass-filtered velocity fields, which are least constrained in the interpolation originally designed
339 to capture large-scale features (Lebedev et al. 2007).

340 To allow a sharper comparison of the HLCC vertical structure in OFES-Q and YoMaHa'07,
341 enlargements of the spatially-filtered surface and deep zonal currents already shown in Fig. 7 are
342 presented in Fig. 11. Despite the large observational noise, model and observations are generally
343 in good qualitative agreement at the surface in terms of typical amplitudes in the island lee (8-10
344 cm s^{-1} east of 170°W) and location of the HLCC and associated westward jets, with a clear decay
345 and southward shift in the upstream (westward) direction (Figs. 11a, 11b). The simulated
346 currents in the far field are however roughly twice weaker than the observed (typically 2–3 cm s^{-1}
347 1 and 4–6 cm s^{-1} west of 170°E , respectively) and tend to be broader than the observed estimates.
348 This suggests a stronger decay in the model, although the low signal-to-noise ratio of the
349 YoMaHa'07 data does not allow to draw any firm conclusions. On the other hand, the observed
350 deep eastward jet appears to strengthen west of $\sim 170^\circ\text{E}$ and is stronger than the modeled
351 counterpart there (which may be partly related to temporal sampling – see appendix B), whereas
352 the modeled one is more zonally uniform with a few meanders (Figs. 11c, 11d). Moreover, the
353 observed flow is patchier and less continuous east of $\sim 170^\circ\text{E}$. Despite these differences, the
354 coincidence of their positions and zonal orientations is remarkable, although with potentially
355 large error in the YoMaHa'07 flow field (appendix B), their correspondence is not conclusive.

356 It is also worth noting that the qualitative consistency with the idealized model results does
357 not prove unequivocally that the far-field deep jet-like velocities are the result of the β -plume
358 dynamics described in this study. Indeed, it is possible that the mean deep eastward flow
359 maximum near 160°E is simply associated to the surface flow maximum at the same longitude
360 (Figs. 7c, 7d, 11b, 11d), both being signatures of energetic mesoscale eddies for instance.
361 However, this hypothesis appears less likely because far-field surface and deep flows are poorly
362 correlated: unlike the mean deep flow, the mean surface flow does not feature a zonally-coherent

363 band of elevated velocities at 145°E-165°E, but a rather patchy structure (Figs. 7c, 7d, 11b, 11d).
364 The same conclusion holds for the spatially highpass-filtered maps of zonal current standard
365 deviation at the surface (not shown) and at 1000 m (not shown but essentially identical to Fig.
366 B2b due to the absence of deep large-scale flow). Another possibility is that the far-field surface
367 and/or deep jets may be associated to striations unrelated to the island-induced wind stress curl
368 forcing. Although plausible given the ubiquity of quasi-zonal jet-like structures (Maximenko et
369 al. 2008), including some clear signals seen closer to the equator in both model and Argo data
370 (Figs. 7b, 7d), this explanation seems unlikely because the far-field jets are located right along
371 the axis of the surface HLCC. In addition, unlike the OFES-Q outputs, the YoMaHa'07 data
372 shows no evidence of such striations to the east of the islands, which is probably because they
373 are weak and somewhat noisy even in altimetric data (Maximenko et al. 2008). This casts doubt
374 on whether such weak signals may leave such a clear signature in the time-mean deep flow west
375 of Hawaii (Fig. 7d). Besides, the deep tropical jets are zonally-coherent across the whole basin in
376 both YoMaHa and OFES-Q (Figs. 7b, 7d), unlike the deep jet west of Hawaii. Noteworthy, the
377 far-field deep jet at 145°E-165°E appears as perhaps the most clearly defined extratropical quasi-
378 zonal jet at 1000 m depth in the YoMaHa'07 dataset globally (Ascani et al. 2010; their Fig. 2).

379 To the best of our knowledge, a deep HLCC extension, reaching 1000 m depth, has not been
380 discussed previously, although fragmentary hints on such deepening can be found in published
381 material. For example, *in situ* data collected along meridional transects west of Hawaii show a
382 westward deepening of the HLCC (Qiu and Durland 2002), although these observations are
383 limited to two sections conducted at 165°W (in September–November 1994) and 179°E (in July–
384 August 1993) and do not extend below 250 m depth. In addition, a deep (450–1100 m) HLCC
385 extension was also found in a 4½-layer model by McCreary et al. (2007).

386

387 **4. Theory**

388 The westward reduction in vertical shear, which takes place in both the idealized β -plume
389 simulations and the HLCC, suggests a possible damping of baroclinic Rossby waves with a
390 preference for higher-order vertical modes. Without nonlinearities in the ROMS model, such
391 damping must be due to vertical mixing of density (diffusion, κ) or momentum (viscosity, ν) or
392 both. A test run with κ increased by an order of magnitude, shows that the flow vertical structure
393 is indeed sensitive to κ (Fig. 3c): changes in the zonal direction take place over much shorter
394 distances than in the control run (Fig. 3a). On the other hand, the baroclinic flow is even more
395 sensitive to ν (Fig. 3d): zonal scales are smaller when viscosity is increased by a factor of 10 than
396 when diffusion is increased by a factor of 10 (Fig. 3c). Other experiments in which κ and ν are
397 separately reduced by a factor of 10 exhibited consistent results, i.e., larger zonal scales for the
398 baroclinic flows, especially when viscosity is reduced (not shown). Thus, the model is sensitive
399 to mixing strength for a realistic range of values, and so suggests that both vertical viscosity and
400 diffusion may have important effects on the flow structure in the real ocean. Given that vertical
401 viscosity is not usually important for the large-scale ocean circulation below the Ekman layer,
402 such strong sensitivity to viscosity is surprising.

403 A linear continuously-stratified (LCS) model (*e.g.*, McCreary 1981; Appendix C) provides a
404 useful framework for understanding the basic properties of our solutions. In this model, solutions
405 are represented as expansions in a complete set of barotropic and baroclinic modes. For our
406 purposes, the key simplifying assumptions are that the background Väisälä frequency N depends
407 only on z , and that

$$408 \quad \nu = A/N^2 \quad \text{and} \quad \kappa = A/(\sigma N^2), \quad (2)$$

409 where $\sigma = \nu/\kappa$ is the Prandtl number and A is a constant, so that the mixing coefficients vary with
 410 depth. Since ν and κ are constant in our numerical solutions, we evaluate the LCS equations for
 411 constant N , using a typical value in the interior ocean (e.g., 10^{-4} s^{-1} for the subtropical North
 412 Pacific).

413 Solving equations (C9) for a single equation in p_n alone gives the quasi-geostrophic potential
 414 vorticity equation (Appendix C)

$$415 \quad \frac{\nu N^2}{c_n^2} (p_{nxx} + p_{nyy}) - \frac{\kappa N^2 f^2}{c_n^4} p_n + \beta p_{nx} = \rho_b f (G_{nx} - F_{ny}) \quad (3)$$

416 where p_n is the expansion coefficient of the pressure p , c_n is the phase speed of the n th mode
 417 gravity wave, F_n and G_n describe how zonal and meridional wind stress couple to each mode,
 418 and subscripts x and y indicate a partial derivative with respect to x and y , respectively. Solutions
 419 to (3) provide the p_n field of the β -plume forced by the winds.

420 The ν - and κ -terms on the left-hand side of (3) determine the westward decay of the plume
 421 due to vertical mixing. An estimate of the relative importance of diffusion versus viscosity in the
 422 decay is the ratio of the first two terms in (3),

$$423 \quad M_n \approx 4R^2 / \pi^2 \sigma R_n^2 \quad (4)$$

424 where $R_n = c_n/f = c_1/(nf)$ is the n th deformation radius and R is the horizontal scale of the wind
 425 curl (appendix D), chosen here as the distance from zero to maximum wind stress (section 2).

426 According to (4), viscosity (diffusion) determines the decay when $M_n \ll 1$ ($M_n \gg 1$), that is,
 427 the forcing has a meridional scale R that is small (large) compared to the deformation radius R_n
 428 times $\pi\sqrt{\sigma}/2$ (which is ~ 5 when $\sigma = 10$, the value used in ROMS and a reasonable estimate for
 429 the real ocean - Pedlosky 1996). Note that M_n scales like n^2 so that, even if $M_1 \ll 1$, M_n will be

430 much greater than 1 for n larger than a critical value n_0 . In the ROMS simulations, we estimate
 431 $M_1 \approx 0.04$ and $n_0 \approx 6$ (Table 1), which explain why the baroclinic flow is sensitive to both κ (Fig.
 432 3c) and ν (Fig. 3d), but more so to the latter. In the OFES solutions, assuming an average value
 433 of $\sigma \sim 10$ (σ varies much with the KPP formulation), M_1 has larger values but still smaller than
 434 one, while n_0 is strictly larger than one (Table 1). Thus, while vertical diffusion likely plays a
 435 more important role in the OFES HLCC compared to the idealized simulations, vertical viscosity
 436 is still the dominant mixing process responsible for the HLCC westward deepening. On the other
 437 hand, the 1° QuikSCAT data used to force OFES (Sasaki et al. 2010) exhibit only one curl dipole
 438 near Hawaii (Fig. 8b), whereas 0.25° data have dipoles in the lee of each island (Chavanne et al.
 439 2002; Yoshida et al. 2011). Using the same method, we estimate $M_1 \approx 0.02$ and $n_0 \approx 8$ (Table 1),
 440 so that the effect of viscosity likely dominates largely that of diffusion in the real HLCC, similar
 441 to the idealized simulations.

442 Equation (3) may also be used to estimate the zonal decay scale associated with each
 443 baroclinic mode when either viscosity or diffusion dominates. Specifically,

$$444 \quad L_\nu = \frac{4\beta R^2 c_1^2}{\pi^2 \nu n^2 N^2} \quad \text{and} \quad L_\kappa = \frac{\beta c_1^4}{\kappa f^2 n^4 N^2} \quad (5)$$

445 are the e-folding zonal scales for viscosity and diffusion, respectively (appendix D). According
 446 to (5), the scales are smaller when mixing is enhanced (Figs. 3c, 3d), and they decrease with
 447 increasing n (preferential damping of higher-order modes). Furthermore, L_ν increases
 448 quadratically with the meridional scale of the forcing, R , whereas L_κ does not vary with R .

449 This latter statement arises from the fact that the κ -term in (3) is directly proportional to p_n ,
 450 whereas the ν -term involves the second meridional derivative of p_n . It is useful to go back to the
 451 vertical mode primitive equations (C9) to understand the origin of such different relationships to
 452 the meridional dimension (appendix C). The first meridional derivative of the ν -term in the zonal

453 momentum equation (involving u_n) appears as a result of the computation of a vorticity equation
454 from both momentum equations. The second meridional derivative of p_n is then obtained through
455 the quasi-geostrophic approximation. Hence, the ν -term in the quasi-geostrophic potential
456 vorticity equation (3) represents the curl of viscosity, which is also the vertical gradient of the
457 curl of the fluid turbulent stress. On the other hand, the computation of the vorticity equation also
458 leads to the consideration of horizontal divergence, *i.e.*, vortex stretching, in the plume
459 dynamics. For each vertical mode, vortex stretching is directly proportional to w_n as seen in the
460 fourth equation of (C8). The κ -term in (3) then originates from the density equation relating p_n to
461 w_n (fourth equation of (C9)).

462 In other words, the κ -term or vortex stretching directly acts on pressure perturbation and does
463 not depend on the scale of the perturbation, *i.e.*, on the scale of the forcing. Conversely, the ν -
464 term or vertical gradient of the curl of the fluid turbulent stress acts on vorticity perturbation.
465 This means that within the quasi-geostrophic approximation, it acts on the horizontal derivatives
466 of the gradient of pressure perturbation, and particularly on the second meridional derivative as a
467 consequence of the anisotropy of the β -plume. Thus, the ν -term is enhanced (quadratically) for
468 small meridional scales of the pressure perturbation, *i.e.*, for small meridional scales of the
469 forcing.

470 To verify the relevance of these theoretical considerations to our idealized experiments, we
471 obtained an additional simulation similar to the control run except with a forcing scale and
472 amplitude of the wind twice as large ($R = 80$ km and $\tau_{max} = 2 \cdot 10^{-5}$ N m⁻²), so that the curl
473 amplitude is unchanged. Fig. 3b confirms that, consistent with the above theory, baroclinic zonal
474 scales are larger for larger forcing scales. In addition, the differences in the surface HLCC zonal
475 extent in OFES-N and OFES-Q (Figs. 8c, 8d) also agree with theoretical predictions.

476 Note that the theoretical R^2 dependence in (5) suggests that with $R = 40$ km in high-resolution
477 scatterometer data (Chavanne et al. 2002; Yoshida et al. 2011), the zonal damping scale may be
478 smaller in the real HLCC compared to OFES, and hence that the real HLCC deepening may be
479 steeper than in the OFES simulations. Since the OFES-Q HLCC maximum at 1000 m is already
480 directly below the surface maximum in the immediate lee of the islands (Fig. 6c), this questions
481 the appropriateness of using the YoMaHa'07 signal 40 degrees further west (Figs. 7d, 11d) as the
482 proxy for the HLCC deepening. As discussed previously, although not very likely, it is possible
483 that the deep Argo signal in the far field does not represent the hypothesized westward deepening
484 but some other dynamical feature. On the other hand, such observation is qualitatively consistent
485 with both OFES-N and ROMS, and inconsistent only with OFES-Q. Perhaps there is something
486 wrong about the HLCC in OFES-Q: as discussed in appendix B, OFES-Q does not reproduce
487 well the observed HLCC interannual variability (Sasaki et al. 2010). One possible explanation is
488 that OFES-Q might simulate SST fields that are inconsistent with the small-scale air-sea
489 interaction over the real ocean and hence with the QuikSCAT wind forcing, leading to unrealistic
490 behavior in the ocean circulation, a problem discussed by Chelton and Xie (2010), and references
491 therein. Given the importance of air-sea feedbacks in the HLCC dynamics (Xie et al. 2001) and
492 the fact that OFES-Q is the only model that implicitly accounts for such interaction in the present
493 study, this hypothesis seems plausible. However, since the deep signal appears farther west in the
494 observation compared to OFES-N (Fig. 5c), and since the larger forcing scale in the latter should
495 produce the opposite effect according to the theoretical considerations presented here, it is also
496 possible that the idealized model is too simplified to account for the complex dynamics of the
497 real HLCC in the presence of fine-scale ocean-atmosphere coupling.

498

499 5. Summary and Discussion

500 5.1 Summary

501 Experiments with an idealized primitive-equation ocean model and an analytical LCS
502 model suggest that the dynamical ocean response to small-scale wind forcing is sensitive to both
503 vertical viscosity and vertical diffusion, which preferentially damp baroclinic Rossby waves
504 associated with higher-order vertical modes. As a result, the β -plume induced by such compact
505 forcing thickens, the surface jet weakens, and the strength of the deep flow increases with
506 distance from the source. In contrast, the barotropic transport remains fairly uniform with
507 longitude, in agreement with the Sverdrup dynamics. Consistent with the LCS theoretical model,
508 due to a dynamically important vertical viscosity, zonal change in the flow vertical structure
509 occurs over a shorter distance for smaller meridional scales of the forcing. A high-resolution
510 OFES simulation forced by reanalyzed winds represents HLCC time-averaged baroclinic and
511 barotropic structures similar to the idealized β -plume. However, when forced by higher-
512 resolution scatterometer winds, the OFES HLCC deep extension does not agree well with the
513 idealized model, possibly because of the distributed forcing along the surface jet axis resulting
514 from air-sea interaction, or because of nonlinear dynamics, eddy fluxes in particular.
515 Nevertheless, the OFES simulations demonstrate the sensitivity of the surface HLCC zonal
516 extent to the wind stress curl forcing scale, as predicted by theory. Whereas our theoretical
517 results are not expected to be quantitatively robust, they are qualitatively useful in that they can
518 help compare numerical solutions with different mixing schemes. Although the LCS, ROMS and
519 OFES models use stratification-dependent, constant, and KPP-derived mixing coefficients,
520 respectively, they exhibit qualitatively similar baroclinic ocean responses to localized forcing
521 and similar sensitivities to the scale of this forcing. On the other hand, the westward decay of the

522 HLCC transport is likely due to the wind stress curl in the far field, though nonlinear stress may
523 also play a role. This decay likely contributes to the surface flow decay, in addition to the effect
524 of the vertical mixing mechanism. The OFES solutions reveal the existence of a deep HLCC
525 extension, which is also found in Argo float trajectory data, although with different
526 characteristics and large uncertainties that do not allow making any firm conclusions. Still, this
527 qualitative agreement supports the relevance of the baroclinic β -plume dynamics to the real
528 ocean and provides new insight into the HLCC mean structure.

529 *5.2 Impact of background currents*

530 Whereas the circulation of the world ocean is characterized by a system of large-scale gyres,
531 effects of the background flow are neglected in the idealized experiments. As discussed in
532 Section 3.2.1, in the case of the Hawaiian Islands, the NEC acts to cancel out the eastward
533 HLCC west of the dateline; moreover, the surface and subsurface branches of the HLCC also
534 appear separated because of the superimposition of the NEC, which has a different vertical
535 structure. It is known that mean flow can affect the propagation characteristics of Rossby waves
536 and eddies (Luyten et al. 1983; Rhines and Young 1982; Chang and Philander 1989), and
537 therefore affect the westward extension of β -plumes. Depending on the strength and direction of
538 the flow, different dynamical effects may be anticipated. A large-scale westward zonal flow such
539 as the NEC, superimposed on the double-gyre response to a curl dipole such as the HLCC, may
540 enhance the westward-flowing jets while having a weak effect on the eastward-flowing jet,
541 which is protected by the island topographic barrier (Liu et al. 2003). The resulting increased
542 meridional shear may then enhance baroclinic and barotropic instabilities and the associated
543 generation of mesoscale eddies (e.g., Yu et al. 2003; Yoshida et al. 2010), which may affect the
544 mean HLCC horizontal and vertical structures since eddies may either draw energy from the

545 mean flow through dissipation (Yu et al. 2003) or reinforce the mean jet through Reynolds shear
546 stress (Lumpkin and Flament 2013). Under certain conditions, the background flow may also be
547 able to advect eddies shed around the islands and accelerate their westward drift (Holland and
548 Mitchum 2001), with potential implications on the plume structure. However, the fact that the
549 HLCC, once isolated from the gyre flow in which it is embedded, compares favorably to the
550 idealized model without background flow is an indication that any interaction between the gyre
551 flow and the HLCC β -plume may be weak.

552 On the other hand, large-scale meridional flow may have different effects. The intrinsic
553 baroclinic instability of meridional flows (Walker and Pedlosky 2002) is a source of nonlinearity
554 that may have an impact on the β -plume. In addition, meridional advection of slow Rossby
555 waves and eddies is expected even for weak flow regimes (Luyten et al. 1983; Rhines and Young
556 1982). Such advection may contribute to the westward HLCC deepening by shifting higher-order
557 baroclinic Rossby waves southward (Qiu and Durland 2002). However, the damping of higher-
558 order baroclinic Rossby waves by vertical mixing is unlikely to be modified by these dynamics:
559 vertical mixing may still be able to damp Rossby waves, whether shifted southward or not.

560 *5.3 Impact of the island mass*

561 In this study, the effect of the island mass on the generation of β -plumes has been neglected.
562 It is however clear that tall, deep water islands such as the Hawaiian islands act as topographic
563 barriers to both the oceanic and atmospheric flows, thus potentially generating localized vorticity
564 in the ocean through both wind and topographic forcings.

565 The effects of the island mass were studied by Qiu and Durland (2002). They used a 2½-
566 layer model in both idealized and realistic configurations to show that the presence of the island
567 mass within the subtropical gyre generates barotropic zonal jets to the west that contribute

568 significantly to the HLCC barotropic transport by reducing it on its southern flank and enhancing
569 it on its northern flank, with an overall 20% reduction in the net transport. The authors do
570 however acknowledge that it may not be the primary forcing of the HLCC. Modelling results
571 obtained with ROMS forced by smooth wind fields have suggested that barotropic zonal jets may
572 also be generated in the lee of tall islands of the southwest Pacific as a result of topographic
573 forcing (Couvelard et al. 2008).

574 The relative importance of the two effects and how they interact is an interesting future
575 study. It has indeed been a subject of controversy in the recent literature. Jiménez et al. (2008)
576 studied the relative importance of these two forcings on eddy shedding by a tall, deep water
577 island in an idealized ocean model on the f -plane (thus not capable of representing β -plume
578 dynamics) applied to the island of Gran Canaria. They found that topographic forcing was a
579 necessary condition for the generation of a Von Karman vortex street in the island lee, and that
580 wind forcing was only required in the case of weak background oceanic flow. Kersalé et al.
581 (2011) performed sensitivity experiments with a realistic configuration of the ROMS model for
582 the Hawaiian islands to infer the relative importance of these two forcings on the generation of
583 mesoscale eddies in the lee of the islands and found qualitatively consistent results with Jiménez
584 et al. (2008). However, Jia et al. (2011) used a similar approach based on the use of the HYCOM
585 model (Bleck 2002) and found opposite results, with a largely dominant role of wind forcing. In
586 agreement with these results, Yoshida et al. (2010) found a close relationship between 60-day
587 Hawaiian lee eddies and high-frequency wind forcing based on satellite data. Interestingly, they
588 also found that 100-day eddy signals that dominate the HLCC region further west (near 165°W)
589 were more likely the result of barotropic instability of the sheared NEC and HLCC.

590 Although these previous works focused on eddy shedding rather than β -plume or HLCC
591 generation, the two questions are related. Indeed, the HLCC is the long-term mean manifestation
592 of westward propagating mesoscale eddies of both signs, anticyclonic to the south and cyclonic
593 to the north (e.g., Holland and Mitchum 2001; Calil et al. 2008). In addition, eddies in both the
594 island lee and the remote region may act as additional sources and sinks of vorticity that can
595 have a significant influence on the time-mean zonal jet as discussed in the previous section.

596 *5.4 Striations*

597 The recent detection of ubiquitous stationary quasi-zonal jet-like structures (striations) in the
598 world ocean (Maximenko et al. 2005, 2008) may indicate that β -plumes survive in most large-
599 scale flows. Indeed, β -plumes have been suggested as a mechanism for the formation of some
600 striations (Centurioni et al. 2008; Hristova et al. 2008; Melnichenko et al. 2010; Wang et al.
601 2012). In particular, striations have been found in both zonal and meridional gyre flows. In
602 subtropical eastern-boundary current regions, they are tilted toward the equator, consistently with
603 the equatorward flow (Maximenko et al. 2008; Melnichenko et al. 2010). Interestingly enough,
604 the HLCC contributes to the global grid of striations, as suggested by Fig. 1a from Maximenko et
605 al. (2008).

606 *5.5 Need for more observations*

607 This study emphasizes the need for high-resolution winds to force ocean models. It also
608 calls for more accurate rates of ocean mixing. For a given forcing, the spatial scales of the β -
609 plume vertical spreading depend on the details of vertical mixing, which in numerical models
610 relies on imperfect parameterizations of subgrid-scale turbulent processes. Likewise, criterion
611 M_n , which depends on the forcing horizontal scale, also depends on the parameterized mixing
612 scheme. In fact, the intensity of eddy-induced vertical mixing may be sensitive to characteristics

613 of the wind forcing, such as high-frequency spectrum as suggested by Cardona and Bracco
614 (2012), and possibly spatial structure as well. Differences in vertical HLCC structure and surface
615 decay between the two OFES solutions may then be partly caused by enhanced eddy mixing in
616 the OFES-Q run associated with the smaller-scale QuikSCAT wind curl dipole. A better
617 knowledge of vertical mixing, which is a main challenge of modern oceanography, is needed for
618 a better modeling of the westward deepening of the HLCC and other wind-driven β -plumes.

619

620

621

APPENDIX A

622

Analytical expression of the barotropic flow

623 To construct the wind-stress vortex that forces the idealized model, we introduce the
624 Gaussian streamfunction,

$$625 \quad \psi_a = R\tau_{\max}\sqrt{e}\exp\left(-\frac{x^2+y^2}{2R^2}\right) \quad (\text{A1})$$

626 The expression for the resulting wind-stress vector $\boldsymbol{\tau}$ is then

$$627 \quad \boldsymbol{\tau} = \mathbf{k} \times \nabla \psi_a, \quad (\text{A2})$$

628 where \mathbf{k} is a unit vector pointing upward. It follows that τ_{\max} is the maximum wind stress, and it
629 occurs at a distance R from the vortex center. The vertical component of wind stress curl
630 (referred in the rest of the paper simply as wind stress curl) is then

$$631 \quad \mathbf{k} \cdot \nabla \times \boldsymbol{\tau} = \frac{\tau_{\max}\sqrt{e}}{R} \left(\frac{x^2+y^2}{R^2} - 2 \right) \exp\left(-\frac{x^2+y^2}{2R^2}\right) \quad (\text{A3})$$

632 The meridional barotropic oceanic flow $V = \frac{\partial \Psi}{\partial x}$ is given by Sverdrup balance (1), where Ψ is
633 the barotropic streamfunction.

634 The zonal barotropic flow U is finally obtained from the depth-integrated continuity equation
 635 by integrating the meridional shear of the meridional barotropic flow zonally from the basin
 636 eastern boundary, yielding

$$637 \quad U = \int_x^{x_e} \frac{\partial V}{\partial y} dx, \quad (\text{A4})$$

638 where x_e is the eastward distance between the vortex center and the eastern boundary.
 639 Substituting V into (A4) and using (A3) gives

$$640 \quad U = \frac{\tau_{\max} \sqrt{e}}{\beta \rho_b R^4} y e^{\frac{-y^2}{2R^2}} \left\{ \sqrt{\frac{\pi}{2}} (3R^2 - y^2) \left[\operatorname{erf}\left(\frac{x_e}{\sqrt{2}R}\right) - \operatorname{erf}\left(\frac{x}{\sqrt{2}R}\right) \right] - R \left(x e^{\frac{-x^2}{2R^2}} - x_e e^{\frac{-x_e^2}{2R^2}} \right) \right\}, \quad (\text{A5})$$

641 where β is the meridional gradient of the Coriolis parameter, ρ_b is the average density of the
 642 water column in the study region, and

$$643 \quad \operatorname{erf}(x) = \frac{2}{\sqrt{\pi}} \int_0^x e^{-t^2} dt \quad (\text{A6})$$

644 is the error function.

645

646

APPENDIX B

647

Errors associated with the YoMaHa'07 velocity estimates

648 The YoMaHa'07 dataset contains both station data, where a surface and a deep velocity
 649 estimate were derived for each Argo float cycle with corresponding geographical coordinates and
 650 time, and the gridded bin-averaged data used in this study, where only mean values, standard
 651 deviation and sample size are available. Thus, when using the gridded data only standard errors
 652 may be explicitly quantified (see below). However, for station data, error estimates in the
 653 individual Argo velocity estimates are provided (Lebedev et al. 2007).

654 The error associated with surface velocity estimates does not include the float slip relative to
655 surrounding water under the joint force of wind and waves. It was estimated with drogued
656 surface drifters (Niiler et al. 1995) to be of the order of a few cm/s under moderate winds, which
657 characterize the trade-wind region west of the Hawaiian Islands. The slip may be stronger for the
658 undrogued Argo floats. The error associated with deep velocity estimates does not account for
659 the real baroclinic velocity structure and does not include variations due to inertial oscillations,
660 among other uncertainties. For more details on the calculation of the surface and deep velocity
661 estimates and associated errors, the reader is invited to refer to Lebedev et al. (2007). With these
662 limitations in mind, it is worth noting that according to Lebedev et al. (2007), both surface and
663 deep velocities are an order of magnitude higher than their respective errors on the global scale.
664 Unfortunately, the authors do not provide the geographical distribution of error estimates.

665 Temporal sampling is another source of uncertainty. Although the YoMaHa'07 dataset
666 covers the 11-year period from 1997 to 2007, the HLCC axis has been sampled without any
667 major spatial gaps only for the 3-year period from 2005 to 2007 (Lebedev et al. 2007; their Fig.
668 6), so the ensemble mean velocities may not be representative of the “true” decadal means. To
669 address questions such as whether the measurements are evenly spaced in time, or whether they
670 are clustered in different time periods at different locations of the HLCC axis, requires a
671 complete analysis of individual Argo float data, which is beyond the scope of the present study.

672 This limits significantly the comparison of the observed ensemble means with the decadal
673 mean simulated by OFES over 1999–2008 (see section 3.2.2). According to altimeter data, 2005
674 was a year of enhanced HLCC velocity east of 170°E, while 2006 and 2007 had HLCC velocity
675 closer to the average over 1993–2007 (Sasaki et al. 2010). On the other hand, the 2005 anomaly
676 is not reproduced in OFES-Q and the model HLCC velocities tend to be weaker than observed

677 over 2000–2007 (Sasaki et al. 2010). This suggests that the YoMaHa’07 ensemble means
678 (OFES-Q decadal means) may overestimate (underestimate) the true decadal means.
679 Unfortunately, the associated uncertainty is hard to quantify, particularly for deep velocities, for
680 which no other observations are available. Therefore, the zonal dependence of surface and deep
681 mean velocities along the HLCC axis in YoMaHa’07 and OFES-Q may only be compared
682 qualitatively and one needs to be cautious even with qualitative comparisons given all the
683 uncertainties of the YoMaHa’07 data.

684 It should also be kept in mind that the YoMaHa’07 velocities are obtained by averaging a
685 scarce ensemble of *in situ* data in a region of strong mesoscale eddy activity (e.g., Calil et al.
686 2008), so the associated uncertainty is large. The standard error associated with the HLCC
687 surface current estimate (Fig. B1c), comparable with the mean value (Fig. 7c), is a result of both
688 scarce data density along the HLCC axis (~20 observations per $1^\circ \times 1^\circ$ grid box over the 11-year
689 period; Fig. B1a) and elevated surface current variability (Fig. B1b), typically $15\text{--}20\text{ cm s}^{-1}$. The
690 error along the HLCC axis is typically $3\text{--}5\text{ cm s}^{-1}$ (Fig. B1c), except between 170°W and 160°W
691 where higher data density (Fig. B1a) allows for a smaller $2\text{--}3\text{ cm s}^{-1}$ error. In the immediate lee
692 of the island, where the HLCC strength reaches 25 cm s^{-1} (Fig. 7c), errors remain relatively
693 small.

694 At 1000 m, the data density pattern is similar to the surface but with fewer observations (Fig.
695 B2a), since many Argo floats are programmed for a different parking depth (Lebedev et al.
696 2007). The error in deep velocities (typically 1 cm s^{-1} ; Fig. B2c) is large compared to the $2\text{--}3\text{ cm}$
697 s^{-1} mean deep currents along the HLCC axis west of 165°E (Fig. 7d). Interestingly, the large-
698 scale variability pattern is very different from that at the surface (Fig. B1b), with larger values in
699 the tropics compared to the subtropics and a clear banded structure south of $\sim 20^\circ\text{N}$ (Fig. B2b)

700 also seen in the mean (Fig. 7d). This is reminiscent of the alternating deep equatorial zonal jets
 701 recently found by Ascani et al. (2010) and by Cravatte et al. (2012) through similar treatments of
 702 Argo float trajectories. Noteworthy, the deep tropical jets are also evident in OFES-Q outputs
 703 (Fig. 7b). This contrast between surface/subsurface flow patterns may result from the strong
 704 signal of the surface-intensified subtropical gyre, which is weak below the thermocline (Figs. 5,
 705 6).

707 APPENDIX C

708 **Quasi-geostrophic potential vorticity equation for the n th vertical mode**

709 Following McCreary (1981), the steady-state hydrostatic linearized primitive equations are

$$\left. \begin{aligned}
 -fv + \frac{p_x}{\rho_b} &= (vu_z)_z \\
 fu + \frac{p_y}{\rho_b} &= (vv_z)_z \\
 p_z &= -\rho g \\
 -\frac{\rho_b}{g} N^2 w &= (\kappa\rho)_{zz} \\
 u_x + v_y + w_z &= 0
 \end{aligned} \right\}, \quad (C1)$$

711 where u , v , and w are the zonal, meridional, and vertical velocity anomalies, respectively, p and ρ
 712 are the pressure and density anomalies, g is the acceleration due to gravity, ρ_b is the average
 713 density of the water column in the study region, and subscripts x , y , and z indicate a partial
 714 derivative with respect to x , y , and z , respectively.

715 The LCS model considers the following rigid-lid surface boundary conditions at $z = 0$

$$716 \quad vu_z = \frac{\tau^x}{\rho_b}, \quad vv_z = \frac{\tau^y}{\rho_b}, \quad w = 0, \quad \rho = 0, \quad (C2)$$

717 and flat-bottom boundary conditions at $z = -D$

718
$$vu_z = v\upsilon_z = w = \rho = 0, \tag{C3}$$

719 where τ^x and τ^y are the zonal and meridional surface wind stress components, respectively.
 720 These are standard boundary conditions, except the assumption of constant background density,
 721 which implies that the atmosphere and the ocean floor act as constant-temperature heat sources.
 722 Whereas the bottom boundary condition generally does not affect the baroclinic flow, which is
 723 mostly confined in the upper-ocean, the surface boundary condition means that the LCS does not
 724 consider any SST anomaly, which limits to some extent the application of the LCS theory to the
 725 real ocean. Both restrictions, however, are necessary for the expansion in vertical modes.

726 Rewriting (C1) with the formulation for mixing coefficients (2) yields

727
$$\left. \begin{aligned} -fv + \frac{p_x}{\rho_b} &= AF(u) \\ fu + \frac{p_y}{\rho_b} &= AF(v) \\ u_x + v_y &= -\frac{A}{\sigma\rho_b} F(F(p)) \\ w &= \frac{1}{N^2} \frac{A}{\sigma\rho_b} [F(p)]_z \\ \rho &= -\frac{p_z}{g} \end{aligned} \right\}, \tag{C4}$$

728 where $F(q) = (q_z/N^2)_z$, and q is u , v , or p .

729 Solutions to (C4) can be expressed in terms of eigenfunctions $\psi_n(z)$ of

730
$$F(\psi_n(z)) = -\frac{\psi_n(z)}{c_n^2}, \tag{C5}$$

731 subject to the boundary conditions that

732
$$\psi_{nz} = 0 \quad \text{at} \quad z = 0 \quad \text{and} \quad z = -D, \tag{C6}$$

733 where c_n is the phase speed of the n th mode gravity wave. A convenient normalization for the
 734 eigenfunctions is

735 $\psi_n(0) = 1.$ (C7)

736 The eigenfunctions are the barotropic ($n=0$) and baroclinic ($n \geq 1$) vertical normal modes of the
 737 system.

738 Solutions can be represented as expansions in the eigenfunctions as follows

739
$$\left. \begin{aligned} u(x, y, z, t) &= \sum_{n=0}^{+\infty} u_n(x, y, t) \psi_n(z) \\ v(x, y, z, t) &= \sum_{n=0}^{+\infty} v_n(x, y, t) \psi_n(z) \\ p(x, y, z, t) &= \sum_{n=0}^{+\infty} p_n(x, y, t) \psi_n(z) \\ w(x, y, z, t) &= \sum_{n=0}^{+\infty} w_n(x, y, t) \int_{-D}^z \psi_n(z) dz \\ \rho(x, y, z, t) &= \sum_{n=0}^{+\infty} \rho_n(x, y, t) \psi_{nz}(z) \end{aligned} \right\}, \quad (C8)$$

740 where u_n , v_n , w_n , p_n , and ρ_n are the expansion coefficients for zonal, meridional, and vertical
 741 velocity components, pressure, and density. Spatial and temporal dependences are omitted
 742 hereafter for clarity.

743 Equations governing the expansion coefficients are found by first substituting u , v , w , p , and
 744 ρ in (C4) by their expressions in (C8). Then, each resulting equation is multiplied by ψ_n and
 745 integrated over the water column. Noting that ψ_n form an orthogonal set, the right-hand sides
 746 are integrated twice by parts. Using boundary conditions (C2), (C3), and (C6), normalization
 747 (C7), and (C5) gives steady-state equations for the expansion coefficients,

748

$$\left. \begin{aligned} -f\mathbf{v}_n + \frac{p_{nx}}{\rho_b} + \frac{vN^2}{c_n^2}u_n &= F_n \\ fu_n + \frac{p_{ny}}{\rho_b} + \frac{vN^2}{c_n^2}v_n &= G_n \\ u_{nx} + v_{ny} + \frac{\kappa N^2}{\rho_b c_n^4}p_n &= 0 \\ w_n &= -\frac{\kappa N^2}{\rho_b c_n^4}p_n \\ \rho_n &= -\frac{p_n}{g} \end{aligned} \right\}, \quad (\text{C9})$$

749 where

750

$$\left. \begin{aligned} F_n &= \frac{\tau^x}{\rho_b \int_{-D}^0 \psi_n^2 dz} \\ G_n &= \frac{\tau^y}{\rho_b \int_{-D}^0 \psi_n^2 dz} \end{aligned} \right\}, \quad (\text{C10})$$

751 describe how the wind forcing couples to each mode.

752 To derive a single equation for p_n , we first subtract the y -derivative of the first equation of
753 (C9) from the x -derivative of the second to get

754

$$f(u_{nx} + v_{ny}) + \beta v_n + \frac{vN^2}{c_n^2}(v_{nx} - u_{ny}) = G_{nx} - F_{ny} \quad (\text{C11})$$

755 We then assume that u_n and v_n are in geostrophic balance in the far field (quasi-geostrophic
756 approximation),

757

$$\left. \begin{aligned} f_0 v_n &\approx \frac{p_{nx}}{\rho_b} \\ f_0 u_n &\approx -\frac{p_{ny}}{\rho_b} \end{aligned} \right\}, \quad (\text{C12})$$

758 where $f = f_0$ in the quasi-geostrophic limit. Substituting (C12) into (C11) and using the third
759 equation of (C9) gives (3), the steady-state response for p_n . Equation (3) is the β -plume quasi-

760 geostrophic potential vorticity balance for each vertical normal mode. It simplifies to (1) for the
 761 barotropic mode ($n = 0$), for which $c_0 \rightarrow \infty$, $\psi_0(z) = 1$, $F_0 = \tau^x/(\rho_b D)$, and $G_0 = \tau^y/(\rho_b D)$.

762

763

APPENDIX D

764

Scaling arguments for viscosity and diffusion

765 Since the zonal scale of a β -plume is large compared to its meridional scale, (3) may be
 766 approximated by

$$767 \quad \frac{N^2}{c_n^2} \left(\nu p_{nyy} - \frac{\kappa}{R_n^2} p_n \right) + \beta p_{nx} = \rho_b f (G_{nx} - F_{ny}), \quad (\text{D1})$$

768 where $R_n = c_n/f = c_1/(nf)$ is the n th deformation radius. Approximating the meridional structure of
 769 the plume by a sine function with a wavelength of $4R$ (Fig. 2a), where R is the distance from
 770 zero to maximum wind stress (Fig. 1), gives

$$771 \quad p_{nyy} \approx -\frac{\pi^2}{4R^2} p_n \quad , \quad (\text{D2})$$

772 and the ratio of the κ -term over the ν -term on the left-hand side of (D1) (or (3)) is then given by
 773 (4). Viscosity (diffusion) dominates in (3) when $M_n \ll 1$ ($M_n \gg 1$).

774 Equation (3) may also be used to estimate the e-folding zonal scale L_n associated with each
 775 baroclinic mode when either viscosity or diffusion dominates. Noting that the zonal plume
 776 structure may be approximated by an exponential decay (Fig. 2c),

$$777 \quad p_{nx} \approx -\frac{p_n}{L_n} \quad , \quad (\text{D3})$$

778 balancing the β -term in (D1) with either the viscous or diffusive term (first two terms on the left-
 779 hand side of (D1)) and using (D2) and (D3) gives (5).

780
781
782
783
784
785
786
787
788
789
790
791
792

Acknowledgements

We are grateful to F. Ascani, B. Qiu, H. Sasaki, S.-P. Xie, and Z. Yu for fruitful discussions. We also wish to thank two anonymous reviewers for helpful comments on an earlier version of this paper. The ROMS simulations were performed on Jaws, a PC cluster at HOSC. The OFES simulations were conducted on the Earth Simulator of the Japan Agency for Marine-Earth Science and Technology (JAMSTEC), and the outputs were accessed via the APDRC, which also provided access to YoMaHa'07 data. This research was partly supported by the JAMSTEC, by NASA through grant NNX07AG53G, and by NOAA through grant NA17RJ1230, which sponsor research at the International Pacific Research Center (IPRC). Additional support was provided by the NASA grants NNX08AR49G and NNX10AE97G. This is the IPRC/SOEST publication #XXXX/YYYY.

793 **References**

- 794 Antonov, J. I., and Coauthors, 2010: *World Ocean Atlas 2009*. NOAA, Washington, D. C.
- 795 Aoki, Y., T. Suga, and K. Hanawa, 2002: Subsurface subtropical fronts of the North Pacific as
796 inherent boundaries in the ventilated thermocline. *J. Phys. Oceanogr.*, **32**, 2299–2311.
- 797 Ascani, F., E. Firing, P. Dutrieux, J. P. McCreary, and A. Ishida, 2010: Deep equatorial ocean
798 circulation induced by a forced-dissipated Yanai beam. *J. Phys. Oceanogr.*, **40**, 1118–1142.
- 799 Bleck, R., 2002: An oceanic general circulation model framed in hybrid isopycnic-Cartesian
800 coordinates. *Ocean Modell.*, **4**, 55–88, doi:10.1016/S1463-5003(01)00012-9.
- 801 Calil, P. H. R., K. J. Richards, Y. Jia, and R. Bidigare, 2008: Eddy activity in the lee of the
802 Hawaiian Islands. *Deep-Sea Res.*, **55**, 1179–1194, doi:10.1016/j.dsr2.2008.01.008.
- 803 Cardona, Y., and A. Bracco, 2012: Enhanced vertical mixing within mesoscale eddies due to
804 high frequency winds in the South China Sea. *Ocean Modell.*, **42**, 1–15,
805 doi:10.1016/j.ocemod.2011.11.004.
- 806 Centurioni, L. R., J. C. Ohlmann, and P. P. Niiler, 2008: Permanent meanders in the California
807 Current System. *J. Phys. Oceanogr.*, **38**, 1690–1710.
- 808 Chang, P., and S. G. H. Philander, 1989: Rossby wave packets in baroclinic mean currents.
809 *Deep-Sea Res.*, **36**, 1, 17–37, doi:10.1016/0198-0149(89)90016-2.
- 810 Chavanne, C., P. Flament, R. Lumpkin, B. Dousset, and A. Bentamy, 2002: Scatterometer
811 observations of wind variations induced by oceanic islands: Implications for wind-driven ocean
812 circulation. *Can. J. Remote Sens.*, **28**(3), 466–474.
- 813 Chelton, D. B., and S.-P. Xie, 2010: Coupled ocean-atmosphere interaction at oceanic
814 mesoscales. *Oceanogr.*, **23**(4), 52–69, doi:10.5670/oceanog.2010.05.

815 —, R. A. deSzoeke, M. G. Schlax, K. El Naggar, and N. Siwertz, 1998: Geographical variability
816 of the first baroclinic Rossby radius of deformation. *J. Phys. Oceanogr.*, **28**, 433–460.

817 —, M. G. Schlax, M. H. Freilich, and R. F. Milliff, 2004: Satellite measurements reveal
818 persistent small-scale features in ocean winds. *Science*, **303**, 978–983,
819 doi:10.1126/science.1091901.

820 Cornillon, P., and K.-A. Park, 2001: Warm core ring velocities inferred from NSCAT. *Geophys.*
821 *Res. Lett.*, **28**, 575–578.

822 Couvelard, X., P. Marchesiello, L. Gourdeau, and J. Lefèvre, 2008: Barotropic zonal jets induced
823 by islands in the Southwest Pacific. *J. Phys. Oceanogr.*, **38**, 2185–2204,
824 doi:10.1175/2008JPO3903.1.

825 Cravatte, S., W. S. Kessler, and F. Marin, 2012: Intermediate zonal jets in the tropical Pacific
826 Ocean observed by Argo floats. *J. Phys. Oceanogr.*, **42**, 1475–1485, doi:10.1175/JPO-D-11-
827 0206.1.

828 Davey, M. K., and P. D. Killworth, 1989: Flows produced by discrete sources of buoyancy. *J.*
829 *Phys. Oceanogr.*, **19**, 1279–1290.

830 Haidvogel, D. B., and P. B. Rhines, 1983: Waves and circulation driven by oscillatory winds in
831 an idealized ocean basin. *Geophys. Astrophys. Fluid Dyn.*, **25**, 1–63.

832 —, and Coauthors, 2008: Ocean forecasting in terrain-following coordinates: Formulation and
833 skill assessment of the Regional Ocean Modeling System. *J. Comput. Phys.*, **227**(7), 3595–
834 3624.

835 Holland, C. L., and G. T. Mitchum, 2001: Propagation of Big Island eddies. *J. Geophys. Res.*,
836 **106**, 935–944, doi:10.1029/2000JC000231.

837 Hristova, H. G., J. Pedlosky, and M. A. Spall, 2008: Radiating instability of a meridional
838 boundary current. *J. Phys. Oceanogr.*, **38**, 2294–2307.

839 Jia, Y., and Coauthors, 2011: Generation of mesoscale eddies in the lee of the Hawaiian islands.
840 *J. Geophys. Res.*, **116**, C11009, doi:10.1029/2011JC007305.

841 Jiménez, B., P. Sangrà, and E. Mason, 2008: A numerical study of the relative importance of
842 wind and topographic forcing on oceanic eddy shedding by tall, deep water islands. *Ocean*
843 *Modell.*, **22**, 146–157, doi:10.1016/j.ocemod.2008.02.004.

844 Kalnay, E., and Coauthors, 1996: The NCEP/NCAR 40-year reanalysis project. *Bull. Amer.*
845 *Meteor. Soc.*, **77**, 437–471.

846 Kelly, K. A., S. Dickinson, M. J. McPhaden, and G. C. Johnson, 2001: Ocean currents evident in
847 satellite wind data. *Geophys. Res. Lett.*, **28**(2), doi:10.1029/2000GL012610.

848 Kersalé, M., A. M. Doglioli, and A. A. Petrenko, 2011: Sensitivity study of the generation of
849 mesoscale eddies in a numerical model of Hawaii islands. *Ocean Sci.*, **7**, 277–291,
850 doi:10.5194/os-7-277-2011.

851 Kessler, W. S., G. C. Johnson, and D. W. Moore, 2003: Sverdrup and nonlinear dynamics of the
852 Pacific equatorial currents. *J. Phys. Oceanogr.*, **33**, 994–1008, doi:10.1175/1520-
853 0485(2003)033<0994:SANDOT>2.0.CO;2.

854 Kida, S., J. F. Price, and J. Yang, 2008: The upper-oceanic response to overflows: A mechanism
855 for the Azores Current. *J. Phys. Oceanogr.*, **38**, 880–895, doi:10.1175/2007JPO3750.1.

856 —, J. Yang, and J. F. Price, 2009: Marginal sea overflows and the upper ocean interaction. *J.*
857 *Phys. Oceanogr.*, **39**, 387–403, doi:10.1175/2008JPO3934.1.

858 Kobashi, F., and H. Kawamura, 2002: Seasonal variation and instability nature of the North
859 Pacific Subtropical Countercurrent and the Hawaiian Lee Countercurrent. *J. Geophys. Res.*,
860 **107**, C11, 3185, doi:10.1029/2001JC001225.

861 Large, W., J. C. McWilliams, and S. Doney, 1994: Oceanic vertical mixing: A review and a
862 model with a nonlocal boundary layer parameterization. *Rev. Geophys.*, **32**, 363–403.

863 Lebedev, K., H. Yoshinari, N. A. Maximenko, and P. W. Hacker, 2007: YoMaHa'07: Velocity
864 data assessed from trajectories of Argo floats at parking level and at the sea surface. *IPRC*
865 *Technical Note*, **4**(2), 16 pp. Available at: <http://apdrc.soest.hawaii.edu/projects/yomaha/>.

866 Liu, Q., S. Wang, Q. Wang, and W. Wang, 2003: On the formation of Subtropical
867 Countercurrent to the west of the Hawaiian Islands. *J. Geophys. Res.*, **108**, 3167,
868 doi:10.1029/2002JC001366.

869 Locarnini, R. A., and Coauthors, 2010: *World Ocean Atlas 2009*. NOAA, Washington, D. C.

870 Lumpkin, R., and P. J. Flament, 2013: Extent and energetics of the Hawaiian Lee
871 Countercurrent. *Oceanogr.*, **26**(1), 58–65, doi:10.5670/oceanog.2013.05.

872 Luyten, J. R., J. Pedlosky, and H. Stommel, 1983: The ventilated thermocline. *J. Phys.*
873 *Oceanogr.*, **13**, 292–309.

874 Masumoto, Y., and Coauthors, 2004: A fifty-year eddy-resolving simulation of the world ocean—
875 Preliminary outcomes of OFES (OGCM for the Earth Simulator). *J. Earth Simulator*, **1**, 35–56.

876 Maximenko, N. A., B. Bang, and H. Sasaki, 2005: Observational evidence of alternating zonal
877 jets in the world ocean. *Geophys. Res. Lett.*, **32**, L12607, doi:10.1029/2005GL022728.

878 —, O. V. Melnichenko, P. P. Niiler, and H. Sasaki, 2008: Stationary mesoscale jet-like features
879 in the ocean. *Geophys. Res. Lett.*, **35**, L08603, doi:10.1029/2008GL033267.

880 McCreary, J. P., 1981: A linear stratified ocean model of the Equatorial Undercurrent. *Philos.*
881 *Trans. Roy. Soc., A*, **298**(1444), 603–635.

882 —, and Coauthors, 2007: Interactions between the Indonesian throughflow and circulations in
883 the Indian and Pacific Oceans. *Prog. Oceanogr.*, **75**, 70–114.

884 Melnichenko, O. V., N. A. Maximenko, N. Schneider, and H. Sasaki, 2010: Quasi-stationary
885 striations in basin-scale oceanic circulation: Vorticity balance from observations and eddy-
886 resolving model. *Ocean Dyn.*, **60**(3), 653–666.

887 Niiler, P. P., A. S. Sybrandy, K. Bi, P. M. Poulain, and D. Bitterman, 1995: Measurements of
888 water-following characteristics of Tristar and Holey-sock drifters. *Deep-Sea Res.*, **42**, 1951-
889 1964.

890 Özgökmen, T. M., E. P. Chassignet, and C. G. H. Rooth, 2001: On the connection between the
891 Mediterranean outflow and the Azores Current. *J. Phys. Oceanogr.*, **31**, 461–480.

892 Pedlosky, J., 1996: *Ocean Circulation Theory*. Springer-Verlag, Berlin, 453 pp.

893 Qiu, B., and T. S. Durland, 2002: Interaction between an island and the ventilated thermocline:
894 Implications for the Hawaiian Lee Countercurrent. *J. Phys. Oceanogr.*, **32**, 3408–3426.

895 —, D. A. Koh, C. Lumpkin, and P. Flament, 1997: Existence and formation mechanism of the
896 North Hawaiian Ridge Current. *J. Phys. Oceanogr.*, **27**, 431–444.

897 Rhines, P. B., 1994: Jets. *Chaos*, **4**, 313–339.

898 —, and W. R. Young, 1982: A theory of wind-driven circulation. I. Mid-ocean gyres. *J. Mar.*
899 *Res.*, **40**, 559–596.

900 Sasaki, H., and M. Nonaka, 2006: Far-reaching Hawaiian Lee Countercurrent driven by wind-
901 stress curl induced by warm SST band along the current. *Geophys. Res. Lett.*, **33**, L13602,
902 doi:10.1029/2006GL026540.

903 —, S.-P. Xie, B. Taguchi, M. Nonaka, and Y. Masumoto, 2010: Seasonal variations of the
904 Hawaiian Lee Countercurrent induced by the meridional migration of the trade winds. *Ocean*
905 *Dyn.*, **60**, 705–715, doi:10.1007/s10236-009-0258-6.

906 Shchepetkin, A. F., and J. C. McWilliams, 2005: The Regional Oceanic Modeling System: A
907 split-explicit, free-surface, topography-following-coordinate ocean model. *Ocean Modell.*, **9**,
908 347–404.

909 Small, R. J., and Coauthors, 2008: Air-sea interaction over ocean fronts and eddies. *Dyn. Atmos.*
910 *Oceans*, **45**, 274–319.

911 Spall, M. A., 2000: Buoyancy-forced circulations around islands and ridges. *J. Mar. Res.*, **58**,
912 957–982.

913 Stommel, H. M., 1982: Is the South Pacific helium-3 plume dynamically active? *Earth Planet.*
914 *Sci. Lett.*, **61**, 63–67.

915 Sverdrup, H. U., 1947: Wind-driven currents in a baroclinic ocean, with application to the
916 equatorial currents of the eastern Pacific. *Proc. Natl. Acad. Sci. U. S. A.*, **33**, 318–326.

917 Walker, A., and J. Pedlosky, 2002: On the instability of meridional baroclinic currents. *J. Phys.*
918 *Oceanogr.*, **32**, 1075–1093.

919 Wang, J., M. A. Spall, G. R. Flierl, and P. Malanotte-Rizzoli, 2012: A new mechanism for the
920 generation of quasi-zonal jets in the ocean. *Geophys. Res. Lett.*, **39**, L10601,
921 doi:10.1029/2012GL051861.

922 Waterman, S., and S. R. Jayne, 2012: Eddy-driven recirculations from a localized transient
923 forcing. *J. Phys. Oceanogr.*, **42**, 430–447.

924 Xie, S.-P., W. T. Liu, Q. Liu, and M. Nonaka, 2001: Far-reaching effects of the Hawaiian islands
925 on the Pacific ocean-atmosphere system. *Science*, **292**, 2057–2060.

926 Yoshida, S., B. Qiu, and P. Hacker, 2010: Wind-generated eddy characteristics in the lee of the
927 island of Hawaii. *J. Geophys. Res.*, **115**, C03019, doi:10.1029/2009JC005417.

928 —, —, and —, 2011: Low-frequency eddy modulations in the Hawaiian Lee Countercurrent:
929 Observations and connection to the Pacific Decadal Oscillation. *J. Geophys. Res.*, **116**,
930 C12009, doi:10.1029/2011JC007286.

931 Yu, Z., N. Maximenko, S.-P. Xie, and M. Nonaka, 2003: On the termination of the Hawaiian Lee
932 Countercurrent. *Geophys. Res. Lett.*, **30**(5), 1215, doi:10.1029/2002GL016710.

Data	Latitude ($^{\circ}$ N)	R_I (km)	R (km)	M_I	n_0
ROMS	30	40	40	0.04	6
OFES-N	20	60	200	0.45	2
OFES-Q	20	60	100	0.11	4
Observed	20	60	40	0.02	8

934 **Table 1.** Relative importance of vertical diffusion versus vertical viscosity in the β -plume
935 westward decay for the first baroclinic mode (M_I) and lowest baroclinic mode order for a
936 dominant vertical diffusion (n_0), estimated for ROMS and OFES, and from 0.25° QuikSCAT
937 observations. An estimated Prandtl number $\sigma \sim 10$ is used for OFES and the observations. See
938 text for details.

939 **Figure 1.** (a) Surface wind stress with maximum at radius $R = 40$ km (location indicated by the
940 meridionally-stretched red circle in Fig. 2a) applied in the box marked in Fig. 2a. (b) Azimuthal
941 wind stress (solid line) and associated wind stress curl (dashed line) and Gaussian streamfunction
942 (dash-dotted line) as a function of radial distance divided by R . Units are (a) 10^{-6} N m^{-2} and (b)
943 10^{-6} N m^{-2} , $10^{-10} \text{ N m}^{-3}$, and 10^{-1} N m^{-1} for wind stress, wind stress curl, and streamfunction,
944 respectively. Contour interval (CI) in (a) is 10^{-6} N m^{-2} .

945

946 **Figure 2.** (a, b) Steady-state barotropic zonal transport per unit width west of the forcing region
947 (a) computed analytically and (b) from ROMS. (c, d) Zonal current from ROMS (c) at sea
948 surface and (d) at 564 m depth. The plots have been stretched meridionally for clarity. The red
949 ellipse and the dashed white box in (a) indicate the location of maximum surface wind stress and
950 the region represented in Fig. 1a, respectively. Units are (a, b) $10^{-2} \text{ m}^2 \text{ s}^{-1}$ and (c, d) 10^{-5} m s^{-1} . CI
951 is (a, b) $4 \cdot 10^{-2} \text{ m}^2 \text{ s}^{-1}$, (c) $4 \cdot 10^{-4} \text{ m s}^{-1}$ and (d) $6 \cdot 10^{-5} \text{ m s}^{-1}$.

952

953 **Figure 3.** (a, b) Steady-state zonal current along the main eastward jet axis from ROMS with $\kappa =$
954 $10^{-5} \text{ m}^2 \text{ s}^{-1}$, $\nu = 10^{-4} \text{ m}^2 \text{ s}^{-1}$, (a) $R = 40$ km and (b) $R = 80$ km. (c, d) Same as (a) but for (c) $\kappa = 10^{-4}$
955 $\text{m}^2 \text{ s}^{-1}$ and (d) $\nu = 10^{-3} \text{ m}^2 \text{ s}^{-1}$. Units are 10^{-5} m s^{-1} . CI is $2 \cdot 10^{-5} \text{ m s}^{-1}$ ($2 \cdot 10^{-4} \text{ m s}^{-1}$) for values below
956 10^{-4} m s^{-1} (above $2 \cdot 10^{-4} \text{ m s}^{-1}$). Values below $2 \cdot 10^{-5} \text{ m s}^{-1}$ are not contoured. Note that the jet axis
957 is shifted northward by 0.2° in (b) as a consequence of the broader wind forcing projected onto
958 the model grid.

959

960 **Figure 4.** Time-mean surface zonal current from (a) OFES-N and (b) OFES-Q over 1999–2008.
961 Units are cm s^{-1} . Solid (dashed) contours are for eastward (westward) current. The thick solid

962 contours are for zero velocity. CI is 5 cm s^{-1} for westward flow and (a) 2 cm s^{-1} , (b) 1 cm s^{-1} for
963 eastward flow. Note the differences in the HLCC zonal extent between the two model solutions.

964

965 **Figure 5.** (a) Zonal current along the HLCC axis in OFES-N, time-averaged over 1999–2008 and
966 meridionally-averaged between 18°N and 20°N . (b, c) Same as (a), except after applying
967 meridional (b) low-pass and (c) high-pass filters (Hann window, see text). The Hawaii Island
968 (Mexico) west coast is located at 156°W (107°W). Units are cm s^{-1} . CI is 1 cm s^{-1} . The 0.5 cm s^{-1}
969 contour is also plotted. The thick solid contours are for zero velocity. Once isolated from the
970 large-scale NEC that dominates zonal flow at intermediate depths, the HLCC appears to have a
971 vertical structure consistent with the idealized β -plume, which includes a deep extension.

972

973 **Figure 6.** Same as Fig. 5, except for OFES-Q averaged meridionally between the thick dashed
974 lines on Figs. 7a, 7b. The transect was chosen to match the axis of the HLCC in OFES-Q. Note
975 the differences in color scales between (c) and Fig. 5c. The near-surface current decay is shorter
976 in OFES-Q compared to OFES-N and the deep eastward flow does not intensify westward.

977

978 **Figure 7.** Meridionally high-pass filtered (Hann window, see text) time-mean zonal current (a) at
979 sea surface and (b) at 1041 m depth (hereafter referred as 1000 m depth) from OFES-Q over
980 1999–2008. (c, d) Same as (a, b), except for Argo float velocities (YoMaHa'07) (c) at sea surface
981 and (d) at 1000 m depth averaged over 1997–2007. Units are cm s^{-1} . CI is (a, c) 5 cm s^{-1} , (b) 0.5
982 cm s^{-1} and (d) 1 cm s^{-1} . Solid (dashed) contours are for eastward (westward) current. The thick
983 solid contours are for zero velocity. The thick dashed lines on (a, b) are used to meridionally-
984 average OFES-Q data as shown on Fig. 6. The thick dashed lines on (c, d) are the same as those

985 on (a, b). The surface flow decay is evident in both OFES-Q outputs and YoMaHa'07 data, but
986 the apparent increasing deep flow west of the islands is not represented in the model.

987

988 **Figure 8.** (a, b) Meridionally high-pass filtered (Hann window, see text) time-mean barotropic
989 zonal transport per unit width (shading and black contours) and time-mean surface wind stress
990 curl dipole around Hawaii (white contours), and (c, d) meridionally high-pass filtered time-mean
991 surface zonal current from (a, c) OFES-N and (b, d) OFES-Q over 1999–2008. Units are (a, b)
992 m^2s^{-1} for transport per unit width and 10^{-7} N m^{-3} for wind stress curl, and (c, d) cm s^{-1} . CI is (a, b)
993 $20 \text{ m}^2\text{s}^{-1}$ for transport per unit width and $5 \cdot 10^{-8} \text{ N m}^{-3}$ for wind stress curl, and (c, d) 5 cm s^{-1} .
994 Solid (dashed) contours are for eastward (westward) flow. The $10 \text{ m}^2\text{s}^{-1}$ contours west of the
995 islands on (a, b) are marked in red to indicate the approximate locations of the HLCC. Note the
996 different color scales in (c, d). The HLCC surface current decay and weaker transport decay in
997 OFES-N are consistent with the idealized β -plume. The surface HLCC zonal extent is larger in
998 OFES-N compared to OFES-Q.

999

1000 **Figure 9.** Time-mean eddy kinetic energy over 1999–2008, computed from the surface
1001 geostrophic flow for (a) OFES-N and (b) OFES-Q. Units are cm^2s^{-2} . CI is $20 \text{ cm}^2\text{s}^{-2}$.

1002

1003 **Figure 10.** Sverdrup zonal transport per unit width derived from the meridionally high-pass
1004 filtered (Hann window, see text) time-mean wind forcing fields over 1999–2008, averaged
1005 meridionally between 18°N and 21°N and between 18.5°N and 19.5°N for OFES-N (thick solid
1006 line) and OFES-Q (thick dashed line), respectively. Total meridionally high-pass filtered time-
1007 mean zonal transport per unit width over 1999–2008, averaged meridionally between 18°N and

1008 21°N and between 18.5°N and 19.5°N for OFES-N (thin solid line) and OFES-Q (thin dashed
1009 line), respectively. The latitude ranges are chosen to capture the HLCC signal in the OFES-N
1010 and OFES-Q Sverdrup flows. The Sverdrup and total OFES-Q transports are also averaged
1011 meridionally between the thick dashed lines on Fig. 7a,b (thick and thin dotted lines,
1012 respectively). Units are m^2s^{-1} . Only eastward transports are represented. For simplicity, the
1013 eastern limit of the zonal integration used in the Sverdrup calculation is taken as 155°W, thereby
1014 ignoring the winds east of the islands, and the presence of islands is also ignored.

1015

1016 **Figure 11.** Comparison of meridionally high-pass filtered (Hann window, see text) time-mean
1017 zonal velocities between OFES-Q averaged over 1999–2008 and Argo float velocities averaged
1018 over 1997–2007 (YoMaHa'07). Surface velocity from (a) OFES-Q and (b) YoMaHa'07; 1000-m
1019 velocity from (c) OFES-Q and (d) YoMaHa'07. (a, b) Same as Figs. 7a, 7c, except enlarged over
1020 the region [150°E-155°W, 16°N-21°N], with color scale over the broader [-15 cm s^{-1} , 15 cm s^{-1}]
1021 range and with CI reduced to 2 cm s^{-1} for eastward velocities lower than 10 cm s^{-1} . (c, d) Same as
1022 Figs. 7b, 7d, except enlarged over the region [150°E-155°W, 16°N-21°N], (d) with color scale
1023 over the broader [-3 cm s^{-1} , 3 cm s^{-1}] range and with CI reduced to (c) 0.2 cm s^{-1} for eastward
1024 velocities, (d) 0.5 cm s^{-1} for eastward velocities lower than 3 cm s^{-1} .

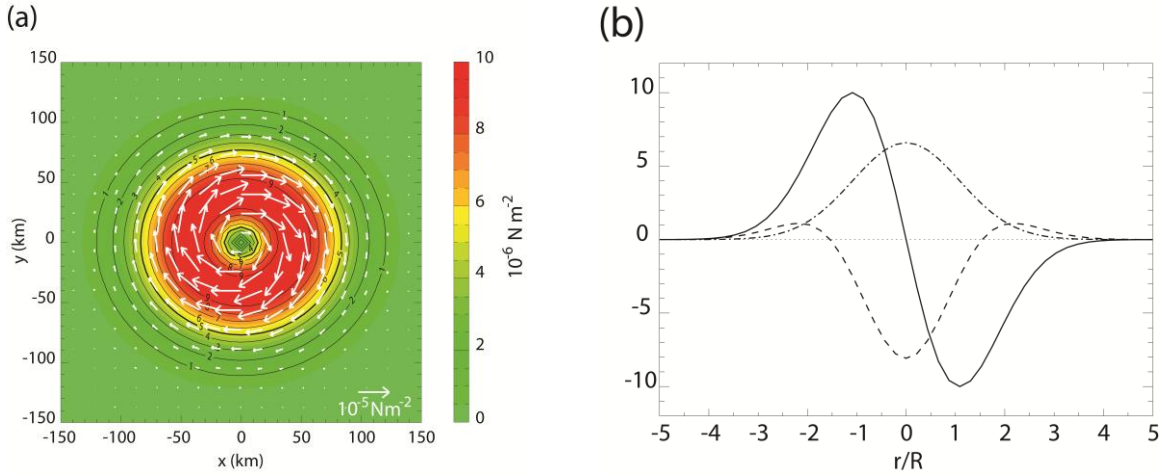
1025

1026 **Figure B1.** (a) Data density (number of observations per $1^\circ \times 1^\circ$ bin), (b) zonal current standard
1027 deviation and (c) standard error of the mean zonal current in the Argo float trajectory data
1028 (YoMaHa'07) at sea surface over 1997–2007. The error is computed as the standard deviation
1029 divided by the square root of the number of observations. Units in (b, c) are cm s^{-1} . CI is (a) 20
1030 and (b, c) 5 cm s^{-1} . The thick dashed lines on all panels are the same as in Fig. 7. Relatively large

1031 error in HLCC mean surface velocities away from the island lee results from both scarce data
1032 density and strong variability. Note that this error estimate does not account for errors in the
1033 individual Argo velocity estimates.

1034

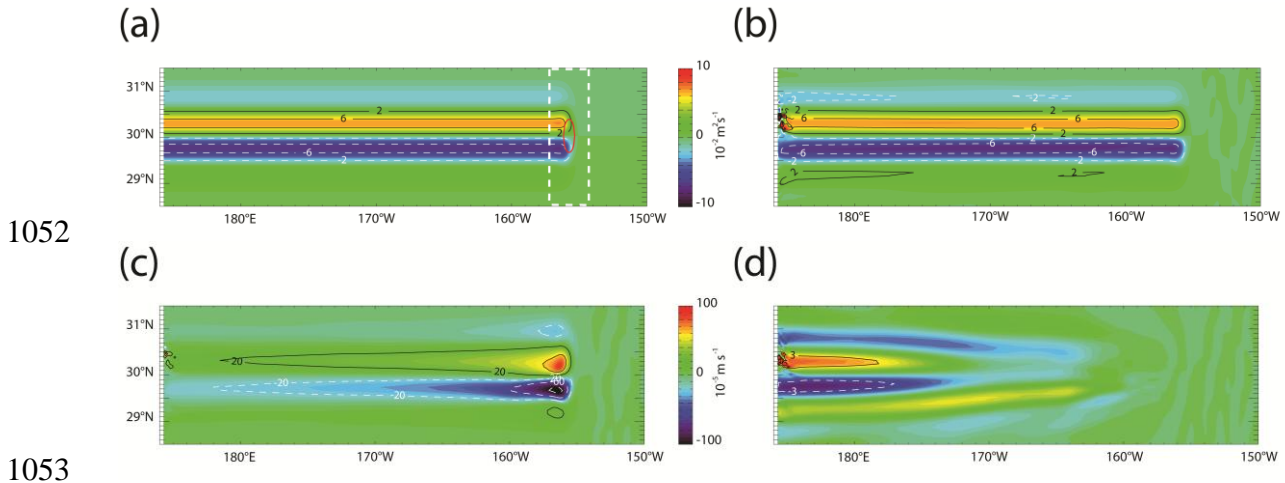
1035 **Figure B2.** Same as Fig. B1, except at 1000 m depth. Note the changes in color bars. CI is (a)
1036 20, (b) 2 cm s^{-1} and (c) 0.5 cm s^{-1} . Large error in HLCC mean deep velocities results from scarce
1037 data density and strong variability. In contrast to the surface, the latter is highest in the tropics
1038 and exhibits a possible deep HLCC extension already seen in the mean. Note that this error
1039 estimate does not account for errors in the individual Argo velocity estimates.



1044

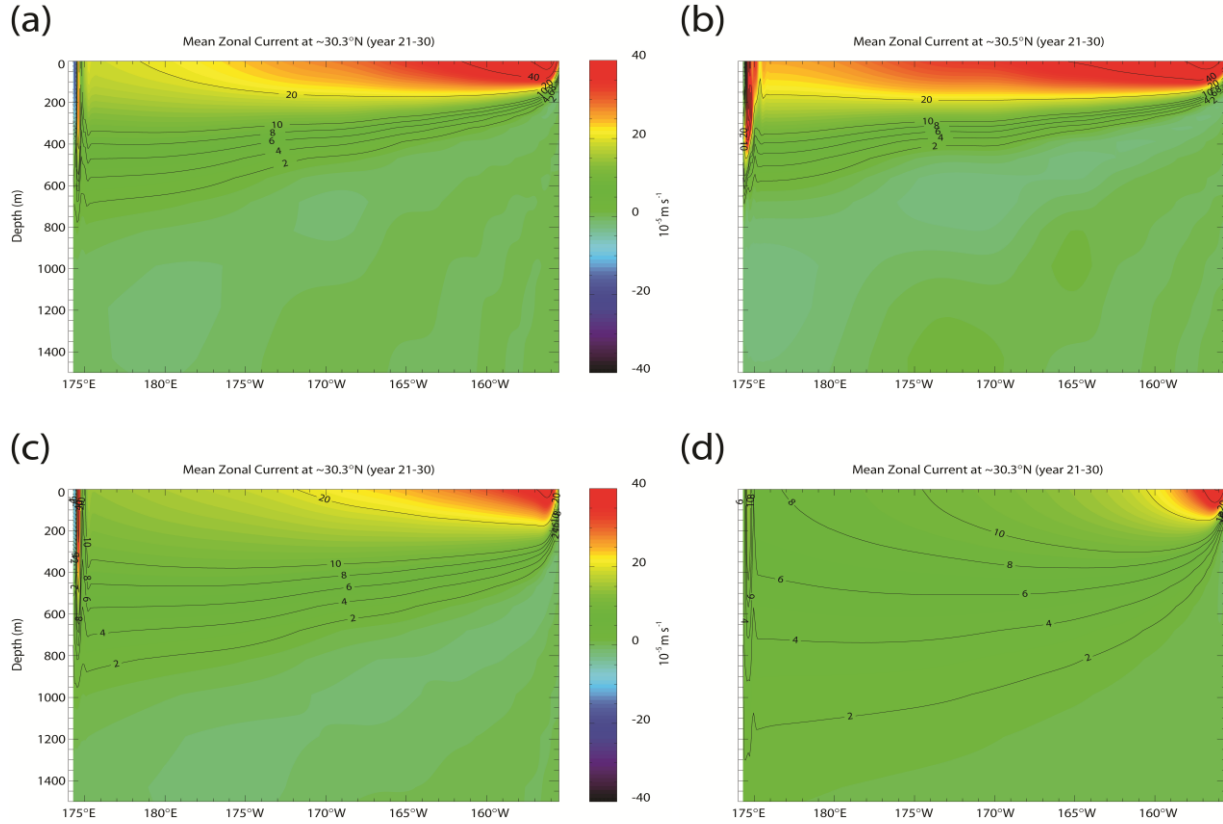
1045 **Figure 1.** (a) Surface wind stress with maximum at radius $R = 40$ km (location indicated by the
 1046 meridionally-stretched red circle in Fig. 2a) applied in the box marked in Fig. 2a. (b) Azimuthal
 1047 wind stress (solid line) and associated wind stress curl (dashed line) and Gaussian streamfunction
 1048 (dash-dotted line) as a function of radial distance divided by R . Units are (a) 10^{-6} N m^{-2} and (b)
 1049 10^{-6} N m^{-2} , $10^{-10} \text{ N m}^{-3}$, and 10^{-1} N m^{-1} for wind stress, wind stress curl, and streamfunction,
 1050 respectively. Contour interval (CI) in (a) is 10^{-6} N m^{-2} .

1051



1052
 1053
 1054 **Figure 2.** (a, b) Steady-state barotropic zonal transport per unit width west of the forcing region
 1055 (a) computed analytically and (b) from ROMS. (c, d) Zonal current from ROMS (c) at sea
 1056 surface and (d) at 564 m depth. The plots have been stretched meridionally for clarity. The red
 1057 ellipse and the dashed white box in (a) indicate the location of maximum surface wind stress and
 1058 the region represented in Fig. 1a, respectively. Units are (a, b) $10^{-2} \text{ m}^2 \text{ s}^{-1}$ and (c, d) 10^{-5} m s^{-1} . CI
 1059 is (a, b) $4 \cdot 10^{-2} \text{ m}^2 \text{ s}^{-1}$, (c) $4 \cdot 10^{-4} \text{ m s}^{-1}$ and (d) $6 \cdot 10^{-5} \text{ m s}^{-1}$.

1060



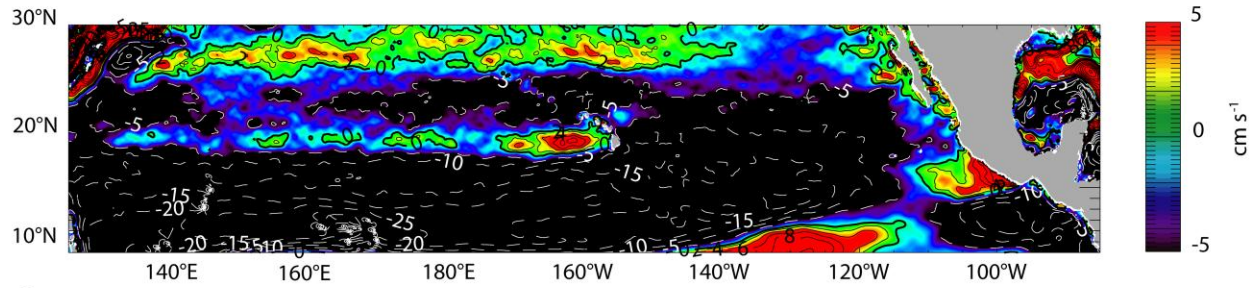
1061

1062

1063 **Figure 3.** (a, b) Steady-state zonal current along the main eastward jet axis from ROMS with $\kappa =$
 1064 $10^{-5} \text{ m}^2\text{s}^{-1}$, $\nu = 10^{-4} \text{ m}^2\text{s}^{-1}$, (a) $R = 40 \text{ km}$ and (b) $R = 80 \text{ km}$. (c, d) Same as (a) but for (c) $\kappa = 10^{-4}$
 1065 m^2s^{-1} and (d) $\nu = 10^{-3} \text{ m}^2\text{s}^{-1}$. Units are 10^{-5} m s^{-1} . CI is $2 \cdot 10^{-5} \text{ m s}^{-1}$ ($2 \cdot 10^{-4} \text{ m s}^{-1}$) for values below
 1066 10^{-4} m s^{-1} (above $2 \cdot 10^{-4} \text{ m s}^{-1}$). Values below $2 \cdot 10^{-5} \text{ m s}^{-1}$ are not contoured. Note that the jet axis
 1067 is shifted northward by 0.2° in (b) as a consequence of the broader wind forcing projected onto
 1068 the model grid.

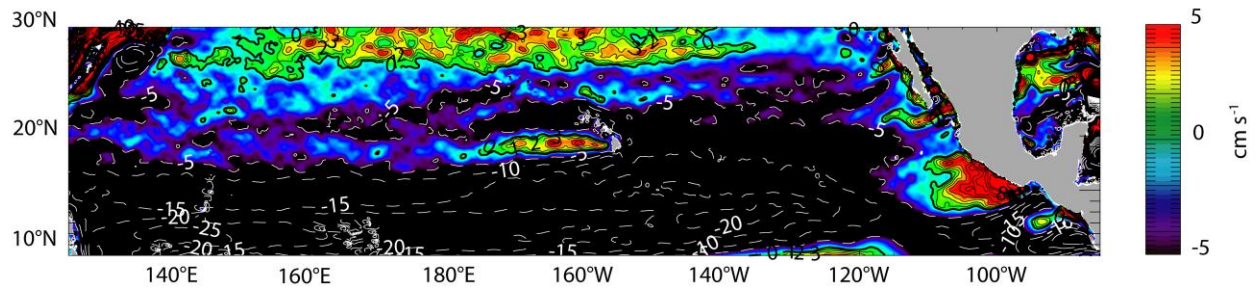
1069

(a)



1070

(b)



1071

1072

Figure 4. Time-mean surface zonal current from (a) OFES-N and (b) OFES-Q over 1999–2008.

1073

Units are cm s^{-1} . Solid (dashed) contours are for eastward (westward) current. The thick solid

1074

contours are for zero velocity. CI is 5 cm s^{-1} for westward flow and (a) 2 cm s^{-1} , (b) 1 cm s^{-1} for

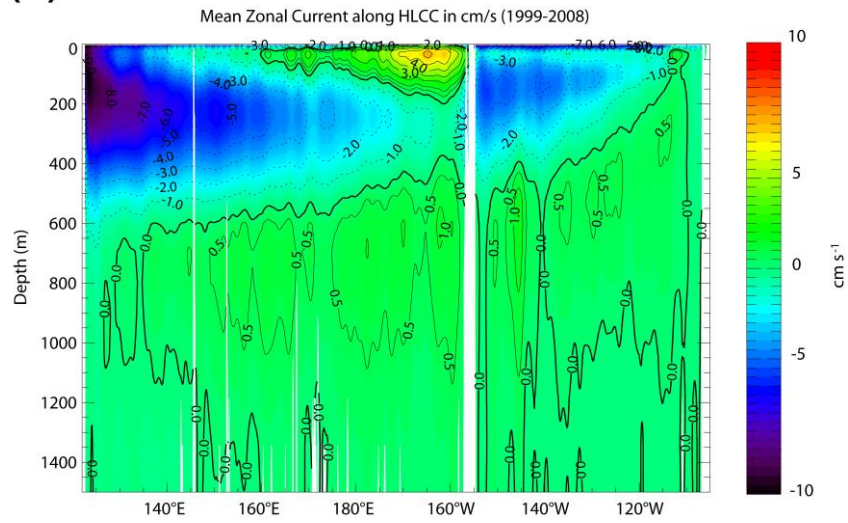
1075

eastward flow. Note the differences in the HLCC zonal extent between the two model solutions.

1076

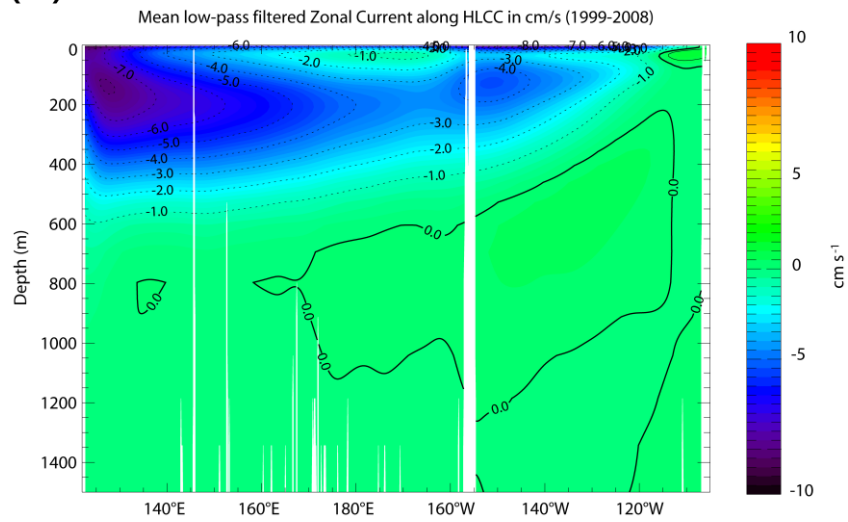
1080 **Figure 5.** (a) Zonal current along the HLCC axis in OFES-N, time-averaged over 1999–2008 and
1081 meridionally-averaged between 18°N and 20°N. (b, c) Same as (a), except after applying
1082 meridional (b) low-pass and (c) high-pass filters (Hann window, see text). The Hawaii Island
1083 (Mexico) west coast is located at 156°W (107°W). Units are cm s^{-1} . CI is 1 cm s^{-1} . The 0.5 cm s^{-1}
1084 contour is also plotted. The thick solid contours are for zero velocity. Once isolated from the
1085 large-scale NEC that dominates zonal flow at intermediate depths, the HLCC appears to have a
1086 vertical structure consistent with the idealized β -plume, which includes a deep extension.
1087

(a)



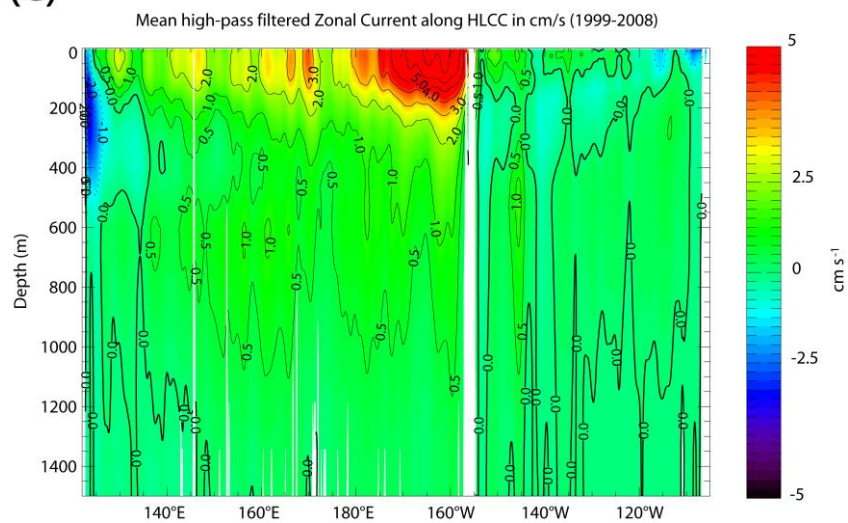
1088

(b)



1089

(c)



1090

1091 **Figure 6.** Same as Fig. 5, except for OFES-Q averaged meridionally between the thick dashed
1092 lines on Figs. 7a, 7b. The transect was chosen to match the axis of the HLCC in OFES-Q. Note
1093 the differences in color scales between (c) and Fig. 5c. The near-surface current decay is shorter
1094 in OFES-Q compared to OFES-N and the deep eastward flow does not intensify westward.
1095

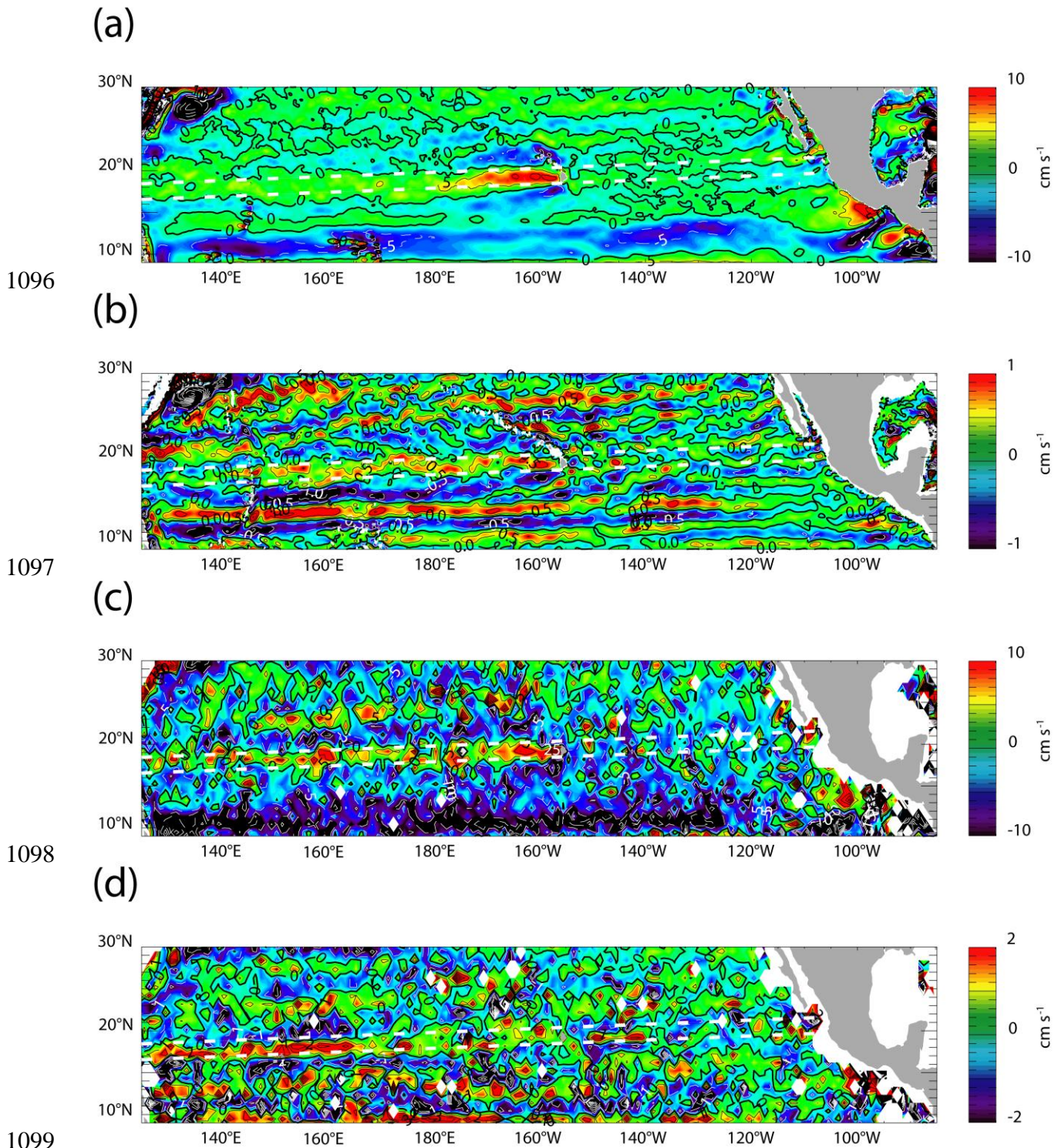
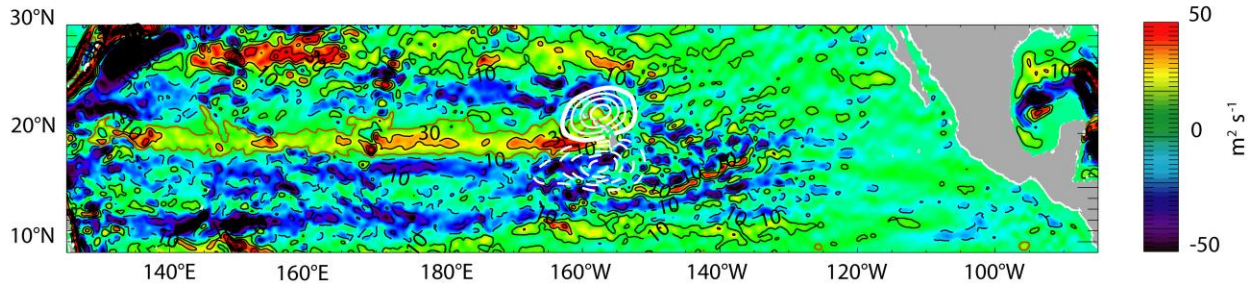


Figure 7. Meridionally high-pass filtered (Hann window, see text) time-mean zonal current (a) at sea surface and (b) at 1041 m depth (hereafter referred as 1000 m depth) from OFES-Q over 1999–2008. (c, d) Same as (a, b), except for Argo float velocities (YoMaHa'07) (c) at sea surface

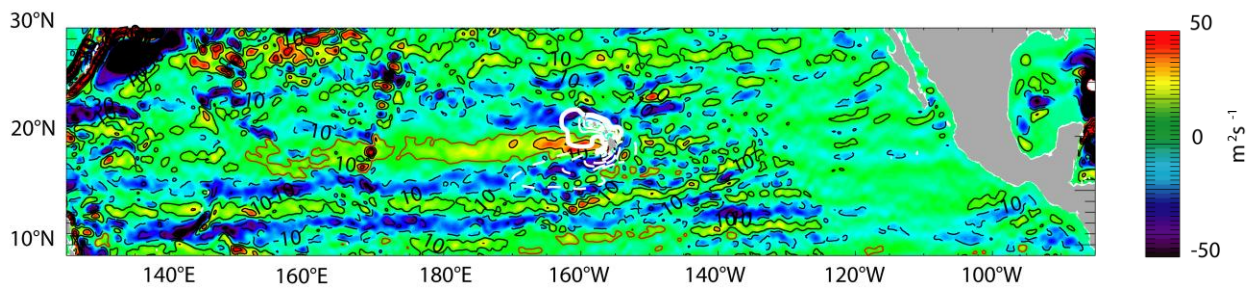
1103 and (d) at 1000 m depth averaged over 1997–2007. Units are cm s^{-1} . CI is (a, c) 5 cm s^{-1} , (b) 0.5
1104 cm s^{-1} and (d) 1 cm s^{-1} . Solid (dashed) contours are for eastward (westward) current. The thick
1105 solid contours are for zero velocity. The thick dashed lines on (a, b) are used to meridionally-
1106 average OFES-Q data as shown on Fig. 6. The thick dashed lines on (c, d) are the same as those
1107 on (a, b). The surface flow decay is evident in both OFES-Q outputs and YoMaHa'07 data, but
1108 the apparent increasing deep flow west of the islands is not represented in the model.
1109

(a)



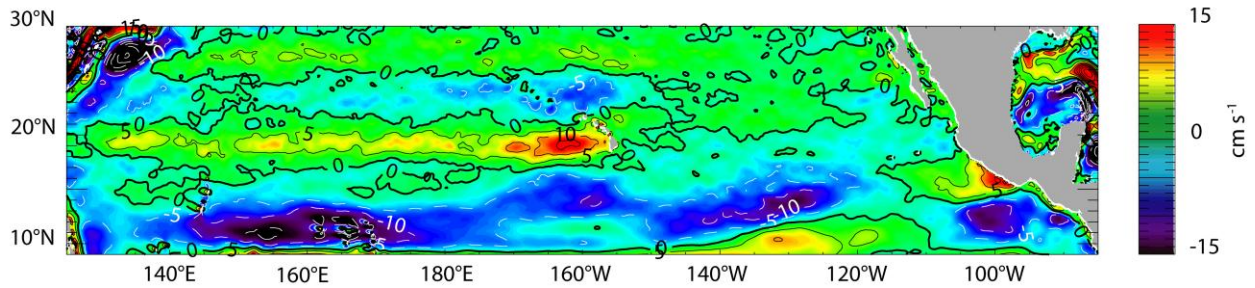
1110

(b)



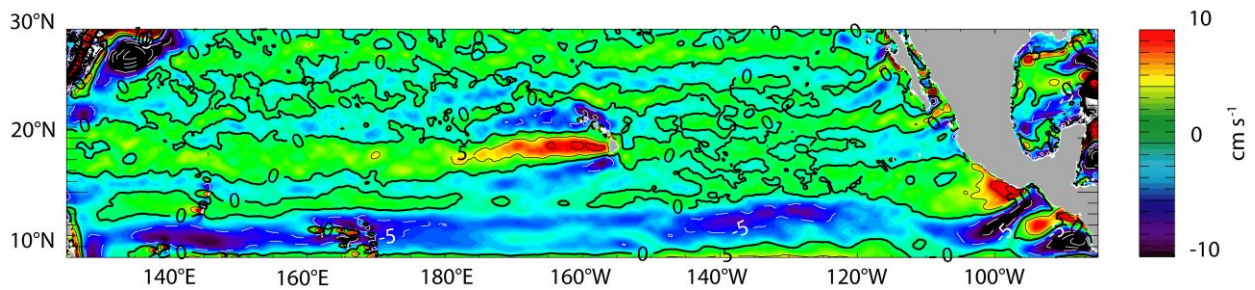
1111

(c)



1112

(d)



1113

1114

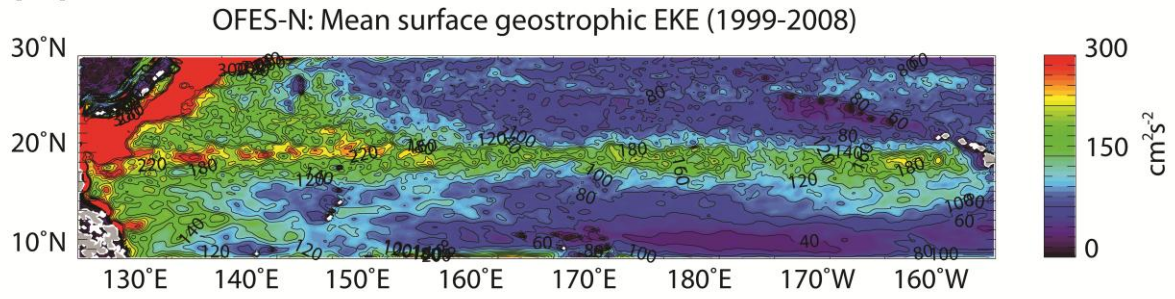
Figure 8. (a, b) Meridionally high-pass filtered (Hann window, see text) time-mean barotropic

1115

zonal transport per unit width (shading and black contours) and time-mean surface wind stress

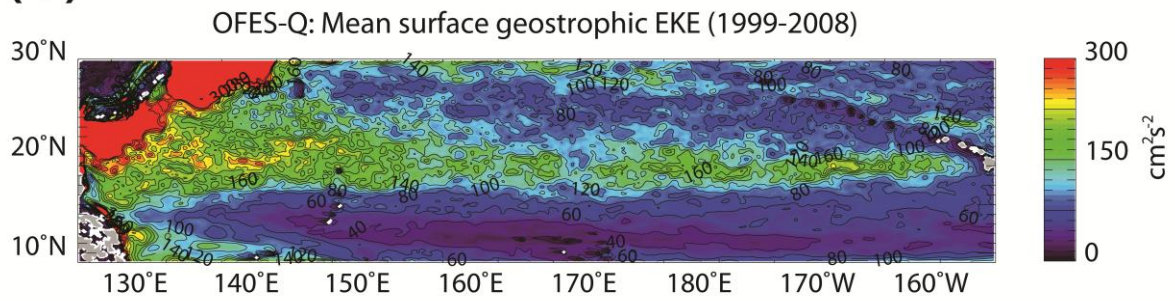
1116 curl dipole around Hawaii (white contours), and (c, d) meridionally high-pass filtered time-mean
1117 surface zonal current from (a, c) OFES-N and (b, d) OFES-Q over 1999–2008. Units are (a, b)
1118 m^2s^{-1} for transport per unit width and 10^{-8} N m^{-3} for wind stress curl, and (c, d) cm s^{-1} . CI is (a, b)
1119 $20 \text{ m}^2\text{s}^{-1}$ for transport per unit width and $5 \cdot 10^{-8} \text{ N m}^{-3}$ for wind stress curl, and (c, d) 5 cm s^{-1} .
1120 Solid (dashed) contours are for eastward (westward) flow. The $10 \text{ m}^2\text{s}^{-1}$ contours west of the
1121 islands on (a, b) are marked in red to indicate the approximate locations of the HLCC. Note the
1122 different color scales in (c, d). The HLCC surface current decay and weaker transport decay in
1123 OFES-N are consistent with the idealized β -plume. The surface HLCC zonal extent is larger in
1124 OFES-N compared to OFES-Q.
1125

(a)



1126

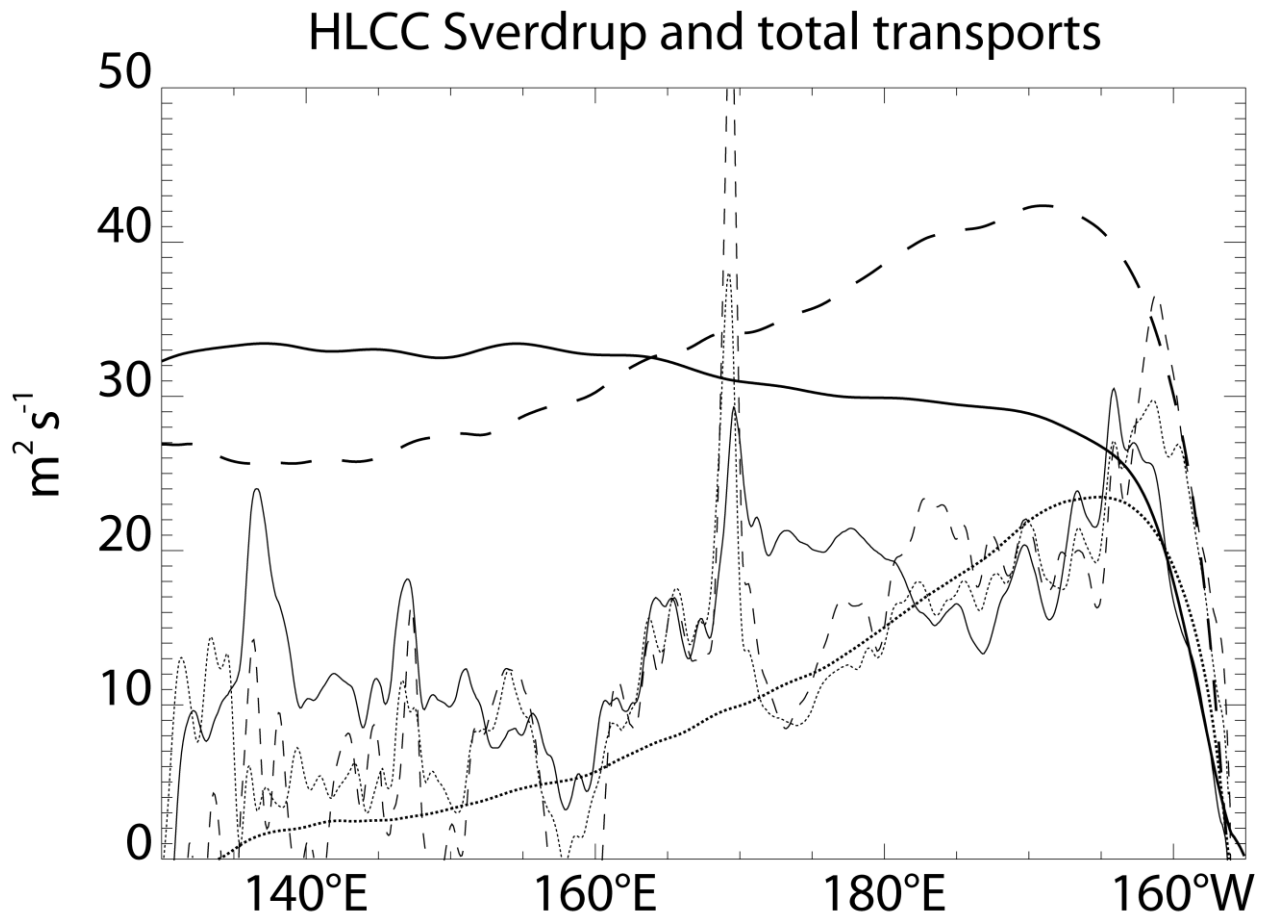
(b)



1127

1128 **Figure 9.** Time-mean eddy kinetic energy over 1999–2008, computed from the surface
1129 geostrophic flow for (a) OFES-N and (b) OFES-Q. Units are cm^2s^{-2} . CI is $20 \text{ cm}^2\text{s}^{-2}$.

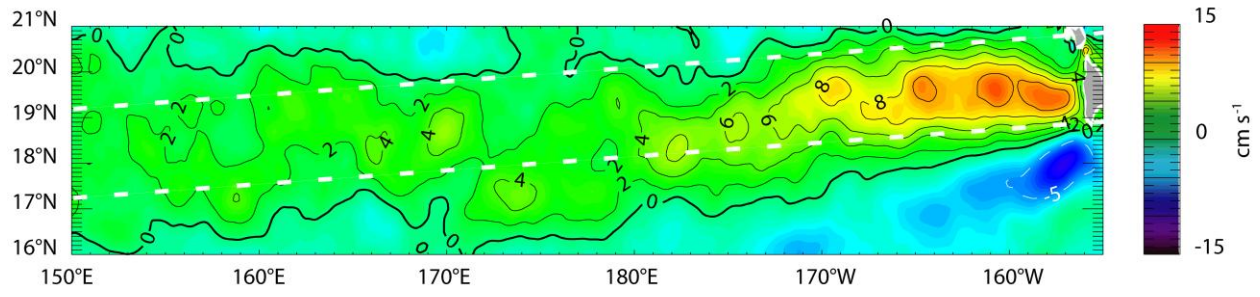
1130



1131
 1132 **Figure 10.** Sverdrup zonal transport per unit width derived from the meridionally high-pass
 1133 filtered (Hann window, see text) time-mean wind forcing fields over 1999–2008, averaged
 1134 meridionally between 18°N and 21°N and between 18.5°N and 19.5°N for OFES-N (thick solid
 1135 line) and OFES-Q (thick dashed line), respectively. Total meridionally high-pass filtered time-
 1136 mean zonal transport per unit width over 1999–2008, averaged meridionally between 18°N and
 1137 21°N and between 18.5°N and 19.5°N for OFES-N (thin solid line) and OFES-Q (thin dashed
 1138 line), respectively. The latitude ranges are chosen to capture the HLCC signal in the OFES-N
 1139 and OFES-Q Sverdrup flows. The Sverdrup and total OFES-Q transports are also averaged
 1140 meridionally between the thick dashed lines on Fig. 7a,b (thick and thin dotted lines,
 1141 respectively). Units are m^2s^{-1} . Only eastward transports are represented. For simplicity, the

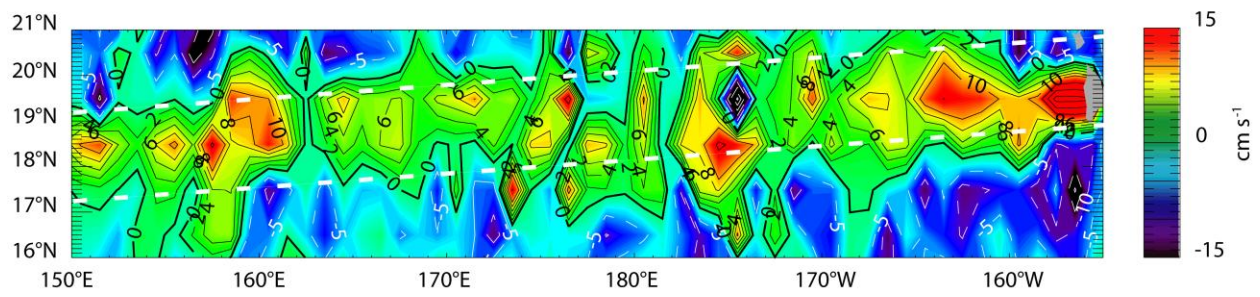
1142 eastern limit of the zonal integration used in the Sverdrup calculation is taken as 155°W , thereby
1143 ignoring the winds east of the islands, and the presence of islands is also ignored.
1144

(a)



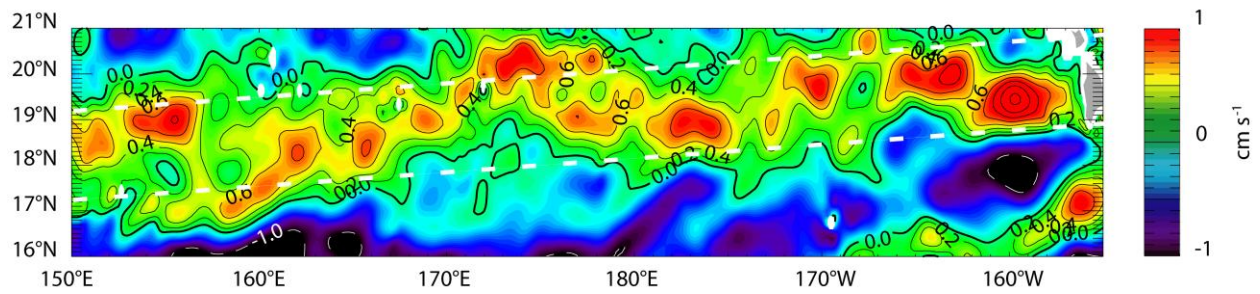
1145

(b)



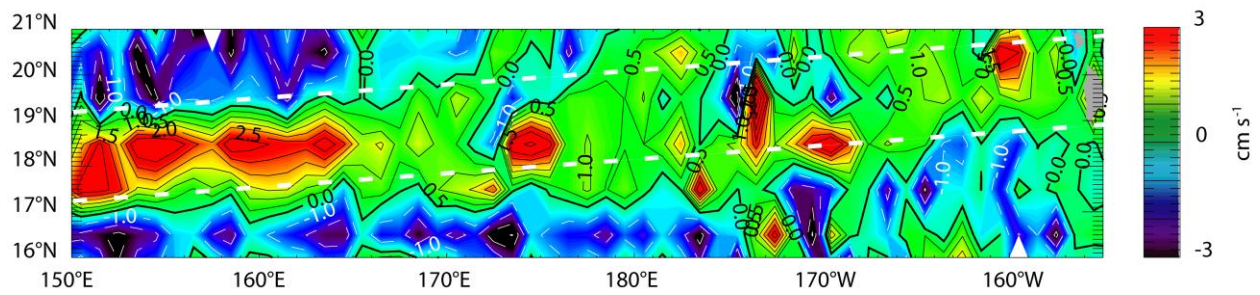
1146

(c)



1147

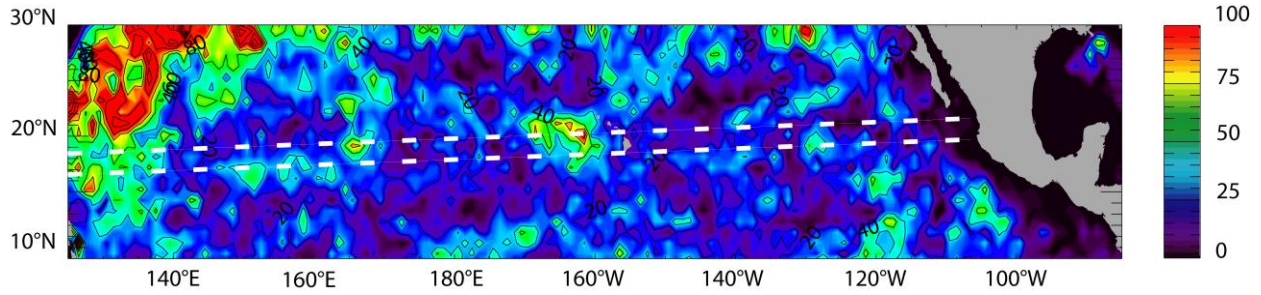
(d)



1148

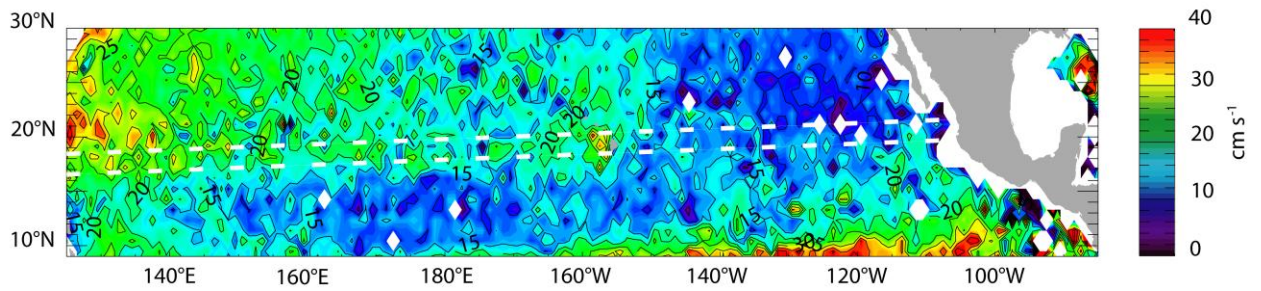
1149 **Figure 11.** Comparison of meridionally high-pass filtered (Hann window, see text) time-mean
1150 zonal velocities between OFES-Q averaged over 1999–2008 and Argo float velocities averaged
1151 over 1997–2007 (YoMaHa’07). Surface velocity from (a) OFES-Q and (b) YoMaHa’07; 1000-m
1152 velocity from (c) OFES-Q and (d) YoMaHa’07. (a, b) Same as Figs. 7a, 7c, except enlarged over
1153 the region [150°E-155°W, 16°N-21°N], with color scale over the broader [-15 cm s⁻¹, 15 cm s⁻¹]
1154 range and with CI reduced to 2 cm s⁻¹ for eastward velocities lower than 10 cm s⁻¹. (c, d) Same as
1155 Figs. 7b, 7d, except enlarged over the region [150°E-155°W, 16°N-21°N], (d) with color scale
1156 over the broader [-3 cm s⁻¹, 3 cm s⁻¹] range and with CI reduced to (c) 0.2 cm s⁻¹ for eastward
1157 velocities, (d) 0.5 cm s⁻¹ for eastward velocities lower than 3 cm s⁻¹.
1158

(a)



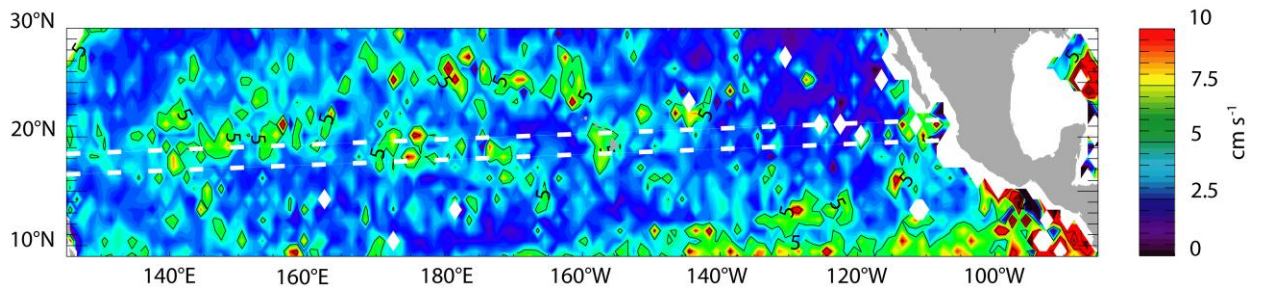
1159

(b)



1160

(c)



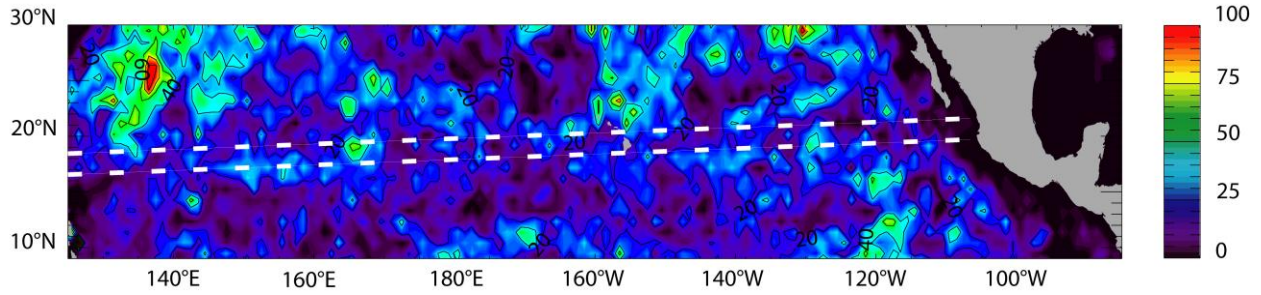
1161

1162 **Figure B1.** (a) Data density (number of observations per $1^\circ \times 1^\circ$ bin), (b) zonal current standard
1163 deviation and (c) standard error of the mean zonal current in the Argo float trajectory data
1164 (YoMaHa'07) at sea surface over 1997–2007. The error is computed as the standard deviation
1165 divided by the square root of the number of observations. Units in (b, c) are cm s^{-1} . CI is (a) 20
1166 and (b, c) 5 cm s^{-1} . The thick dashed lines on all panels are the same as in Fig. 7. Relatively large
1167 error in HLCC mean surface velocities away from the island lee results from both scarce data

1168 density and strong variability. Note that this error estimate does not account for errors in the
1169 individual Argo velocity estimates.

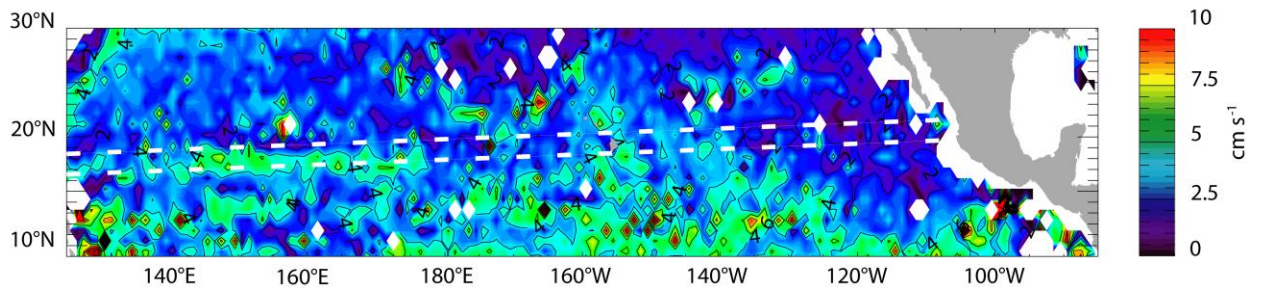
1170

(a)



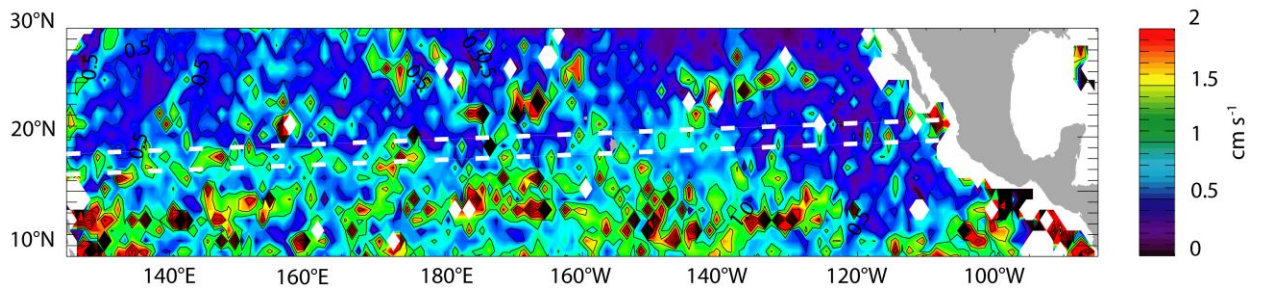
1171

(b)



1172

(c)



1173

1174 **Figure B2.** Same as Fig. B1, except at 1000 m depth. Note the changes in color bars. CI is (a)
1175 20, (b) 2 cm s⁻¹ and (c) 0.5 cm s⁻¹. Large error in HLCC mean deep velocities results from scarce
1176 data density and strong variability. In contrast to the surface, the latter is highest in the tropics
1177 and exhibits a possible deep HLCC extension already seen in the mean. Note that this error
1178 estimate does not account for errors in the individual Argo velocity estimates.